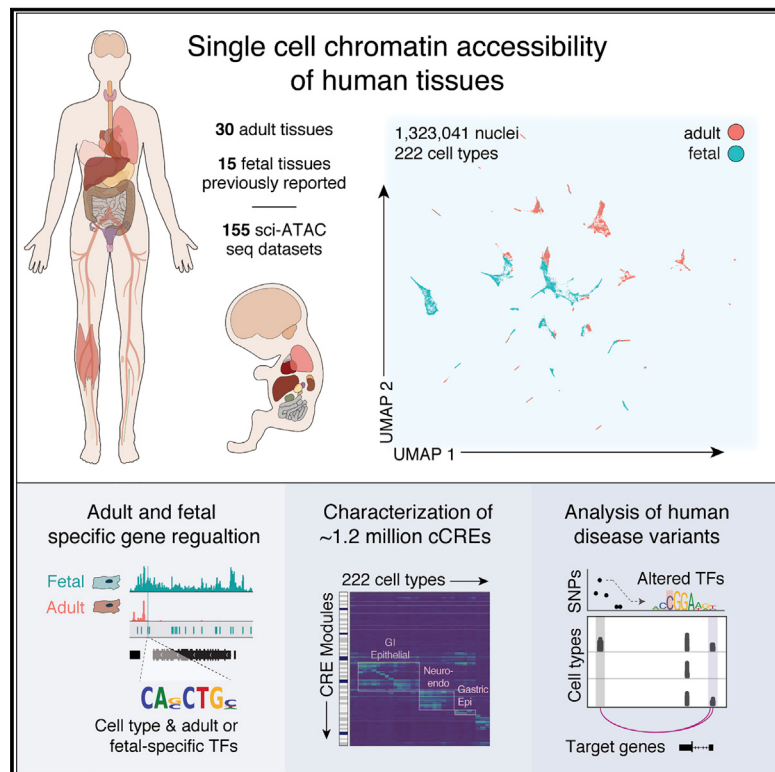


# A single-cell atlas of chromatin accessibility in the human genome

## Graphical abstract



## Authors

Kai Zhang, James D. Hocker,  
Michael Miller, ..., Allen Wang,  
Sebastian Preissl, Bing Ren

## Correspondence

biren@health.ucsd.edu

## In brief

A cell-type-resolved map of human *cis*-regulatory elements, derived from single cell analysis of diverse tissue types, facilitates functional interpretation of the noncoding variants associated with complex human traits and diseases.

## Highlights

- Integrating > 1.3 million single-cell chromatin profiles from adult/fetal human tissues
- An atlas of ~1.2 million candidate *cis*-regulatory elements across 222 cell types
- Cell-type specificity of fetal and adult candidate *cis*-regulatory elements
- Interpretation of noncoding variants associated with complex traits and diseases



## Resource

# A single-cell atlas of chromatin accessibility in the human genome

Kai Zhang,<sup>1,6,8</sup> James D. Hocker,<sup>1,2,3,8</sup> Michael Miller,<sup>4</sup> Xiaomeng Hou,<sup>4</sup> Joshua Chiu,<sup>3,5</sup> Olivier B. Poirion,<sup>4</sup> Yunjiang Qiu,<sup>1</sup> Yang E. Li,<sup>1,6</sup> Kyle J. Gaulton,<sup>5,7</sup> Allen Wang,<sup>4</sup> Sebastian Preissl,<sup>4</sup> and Bing Ren<sup>1,4,6,7,9,\*</sup>

<sup>1</sup>Ludwig Institute for Cancer Research, La Jolla, CA, USA

<sup>2</sup>Medical Scientist Training Program, University of California San Diego, La Jolla, CA, USA

<sup>3</sup>Biomedical Sciences Graduate Program, University of California San Diego, La Jolla, CA, USA

<sup>4</sup>Center for Epigenomics, University of California San Diego, La Jolla, CA, USA

<sup>5</sup>Department of Pediatrics, Pediatric Diabetes Research Center, University of California San Diego, La Jolla, CA, USA

<sup>6</sup>Department of Cellular and Molecular Medicine, University of California San Diego School of Medicine, La Jolla, CA, USA

<sup>7</sup>Institute for Genomic Medicine, University of California San Diego, La Jolla, CA, USA

<sup>8</sup>These authors contributed equally

<sup>9</sup>Lead contact

\*Correspondence: [biren@health.ucsd.edu](mailto:biren@health.ucsd.edu)

<https://doi.org/10.1016/j.cell.2021.10.024>

## SUMMARY

Current catalogs of regulatory sequences in the human genome are still incomplete and lack cell type resolution. To profile the activity of gene regulatory elements in diverse cell types and tissues in the human body, we applied single-cell chromatin accessibility assays to 30 adult human tissue types from multiple donors. We integrated these datasets with previous single-cell chromatin accessibility data from 15 fetal tissue types to reveal the status of open chromatin for ~1.2 million candidate *cis*-regulatory elements (cCREs) in 222 distinct cell types comprised of >1.3 million nuclei. We used these chromatin accessibility maps to delineate cell-type-specificity of fetal and adult human cCREs and to systematically interpret the noncoding variants associated with complex human traits and diseases. This rich resource provides a foundation for the analysis of gene regulatory programs in human cell types across tissues, life stages, and organ systems.

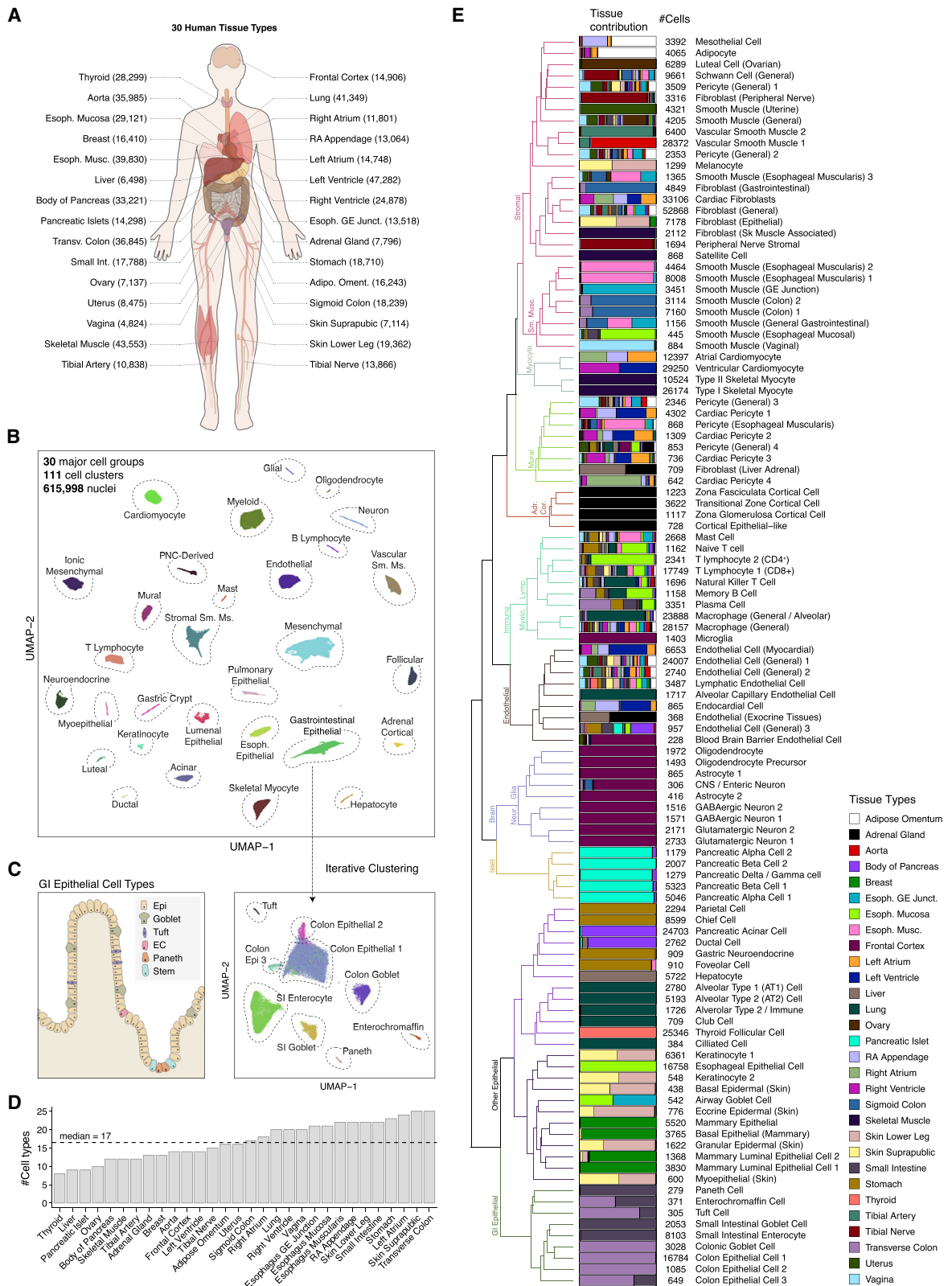
## INTRODUCTION

The human body is comprised of various organs, tissues, and cell types, each with highly specialized functions. The genes expressed in each tissue and cell type—and in turn their physiologic roles in the body—are regulated by *cis*-regulatory elements such as enhancers and promoters (Carter and Zhao, 2021). These sequences dictate the expression patterns of target genes by recruiting sequence-specific transcription factors (TFs) in a cell-type-specific manner (Shlyueva et al., 2014). Upon binding of TFs, *cis*-regulatory elements frequently adopt conformational changes such that they are more accessible to endonucleases or transposases, enabling genome-wide discovery of candidate *cis*-regulatory elements (cCREs) by combining assays incorporating these enzymes with high throughput sequencing (Buenrostro et al., 2013; John et al., 2013; Klemm et al., 2019). However, conventional assays have, in large part, used heterogeneous tissues as input materials to produce population average measurements, and consequently, the current catalogs of candidate regulatory sequences in the human genome (Andersson et al., 2014; Meuleman et al., 2020; Moore et al., 2020; Kundaje et al., 2015; Shen et al., 2012) still lack information about the cell-

type-specific activities of most elements. This limitation has hampered our ability to study gene regulatory programs in distinct human cell types and to interpret the noncoding DNA in the human genome.

Genome-wide association studies (GWAS) have identified hundreds of thousands of genetic variants associated with a broad spectrum of human traits and diseases. The large majority of these variants are noncoding (Claussnitzer et al., 2020). Observations that annotated *cis*-regulatory elements in disease-relevant tissues and cell types are enriched for noncoding disease risk variants (Ernst et al., 2011; Maurano et al., 2012; Kundaje et al., 2015) led to the hypothesis that a major mechanism by which noncoding variants influence disease risk is by affecting transcriptional regulatory elements in specific cell types. However, annotation of these noncoding risk variants has been hindered by a lack of cell-type-resolved maps of regulatory elements in the human genome. Although previous approaches to distinguish causal variants from local variants in linkage disequilibrium (LD) using fine mapping (Wakefield, 2009), and to link variants to target genes using co-accessibility of open chromatin regions in single-cells (Pliner et al., 2018) or 3D chromosomal contact-based linkage scores (Nasser et al., 2021), have made important strides toward the prioritization of causal variants





(legend on next page)

and the prediction of their target genes, functional interpretation of the noncoding variants continues to be challenging.

Single-cell omics technologies, enabled by droplet-based, combinatorial barcoding or other approaches, have now enabled the profiling of transcriptome, epigenome, and chromatin organization from complex tissues at single-cell resolution (Grosselin et al., 2019; Klein et al., 2015; Lake et al., 2018; Luo et al., 2017a; Macosko et al., 2015; Preissl et al., 2018). In particular, combinatorial cellular barcoding-based assays such as sci-ATAC-seq (Cusanovich et al., 2015) have permitted the identification of cCREs in single nuclei without the need for physical purification of individual cell types. The resulting data can be used to deconvolute cell types from mixed cell populations and to dissect cell-type-specific transcriptomic and epigenomic states in primary tissues. Although these tools have been applied to mammalian tissues including murine biosamples (Cusanovich et al., 2018; Lareau et al., 2019; Li et al., 2021; Preissl et al., 2018; Sinnamon et al., 2019), human fetal tissues (Domcke et al., 2020; Trevino et al., 2021), and a few individual adult human organ systems (Chiou et al., 2021; Corces et al., 2020; Hocker et al., 2021; Wang et al., 2020), we still lack comprehensive cell-type-resolved maps of cCREs from most primary tissues of the adult human body.

In the present study, we used a modified sci-ATAC-seq protocol optimized for flash frozen primary tissues (Hocker et al., 2021; Preissl et al., 2018) to profile chromatin accessibility in 30 adult human tissue types from multiple donors. We profiled 615,998 nuclei from these tissues, grouped them into 111 distinct cell types based on similarity in chromatin landscapes, and identified a union of 890,130 open chromatin regions corresponding to cCREs from the resulting maps. We next integrated these data with a recent fetal cell atlas of chromatin accessibility (Domcke et al., 2020) to reveal open chromatin profiles for >1.3 million cells across the human lifespan and chromatin accessibility maps at 1,154,611 cCREs covering 14.8% of the genome for 222 cell types. Finally, we used this cCRE atlas to interpret cell types and target genes for noncoding variants associated with 240 complex human traits and diseases, reveal cell-type-disease associations, and suggest relevant therapeutic targets in human cell types. We created an interactive web atlas to disseminate this resource (*cis*-element ATLAS [CATLAS]; <http://catlas.org/humanenhancer>).

## RESULTS

### Single-cell chromatin accessibility analysis of adult human primary tissues

To generate a cell atlas of cCREs in the adult human body, we performed sci-ATAC-seq (Cusanovich et al., 2015; Preissl et al.,

2018) with primary tissue samples collected from 30 distinct anatomic sites in postmortem adult human donors (Figure 1A; Table S1). Tissue samples were chosen to survey a breadth of human organ systems which differed in their nuclear compositions and sensitivities to mechanical dissociation, posing a technical challenge. We thus optimized nuclear isolation methods and buffer conditions for different tissue types (Table S1; STAR Methods). Subsequently, we generated sci-ATAC-seq datasets using a semi-automated workflow (Hocker et al., 2021; Preissl et al., 2018) and sequenced resulting libraries to 6,464 raw sequence reads per nucleus on average, with a median read duplication rate of 44.88% (Table S2). After filtering out lower quality nuclei and potential doublets, we finally obtained high quality open chromatin profiles for 615,998 nuclei, with a median of 2,822 unique open chromatin fragments per nucleus and an average transcription start site (TSS) enrichment score of 12.8 ( $\pm 3.2$ ) per nucleus (Figure 1B; Table S2; Data S1; STAR Methods).

Analyzing large single-cell chromatin accessibility datasets has been challenging. In the latest development of SnapATAC (Fang et al., 2021), we further improved its scalability to handle millions of cells. Using this algorithm, we first identified 30 major cell groups (Figure 1B), 22 (73%) of which were found to consist of multiple subclusters during a second round of clustering analysis (Methods S1; STAR Methods). Altogether, we uncovered a total of 111 distinct cell clusters (Figures 1B–E).

### Annotation of major and sub-classes of human cell types

To annotate the resulting cell clusters, we first curated a set of marker genes from the PanglaoDB marker gene database (Frantzén et al., 2019) corresponding to expected human cell types. We utilized chromatin accessibility at the promoter as a proxy for gene activity and computed cell-type enrichment scores for each of the 111 clusters to create initial cell cluster annotations (Methods S1; STAR Methods). We next manually reviewed these assignments based on focused consideration of marker gene accessibility (Methods S1). Altogether, we annotated each of the 30 major cell groups and all 111 distinct clusters with a cell type label (Figure 1E; Table S3). For example, within the major cell group of gastrointestinal epithelial cells, higher resolution subclustering and annotation revealed three clusters of colon epithelial cells, one cluster of enterocytes from the small intestine, two clusters of goblet cells from the colon and small intestine, respectively, and three rare populations with distinct chromatin accessibility profiles including enterochromaffin cells (0.060% of total nuclei), tuft cells (0.050% of total nuclei), and Paneth cells (0.045% of total nuclei) (Figures 1B and 1C).

Encouragingly, several prevalent cell types detected in most tissue samples, such as endothelial cells and myeloid cells,

**Figure 1. Single-cell chromatin accessibility analysis of 30 adult human primary tissues**

- (A) A total of 92 biosamples from 30 tissue types, were used for sci-ATAC-seq. The number of nuclei profiled per tissue is denoted in parentheses.
- (B) Clustering of 615,998 nuclei revealed 30 major cell groups. Each dot represents a nucleus colored by cluster ID. Embedding was created by uniform manifold approximation and projection (UMAP) (McInnes et al., 2018).
- (C) An example illustrating subclusters within the major cell group of gastrointestinal (GI) epithelial cells revealed by iterative clustering.
- (D) Bar plot showing the number of cell types identified in each of the 30 human tissues, counting only cell types constituting >0.2% of all cells in the given tissue.
- (E) Distribution of cell types across human tissues. The dendrogram on the left was created by hierarchical clustering of cell clusters based on chromatin accessibility. The bar chart represents relative contributions of tissues to cell clusters. Raw data are available on Mendeley Data (10.17632/yv4fv6cnm.1). See also Tables S1, S2, and S3, Data S1, and Methods S1.

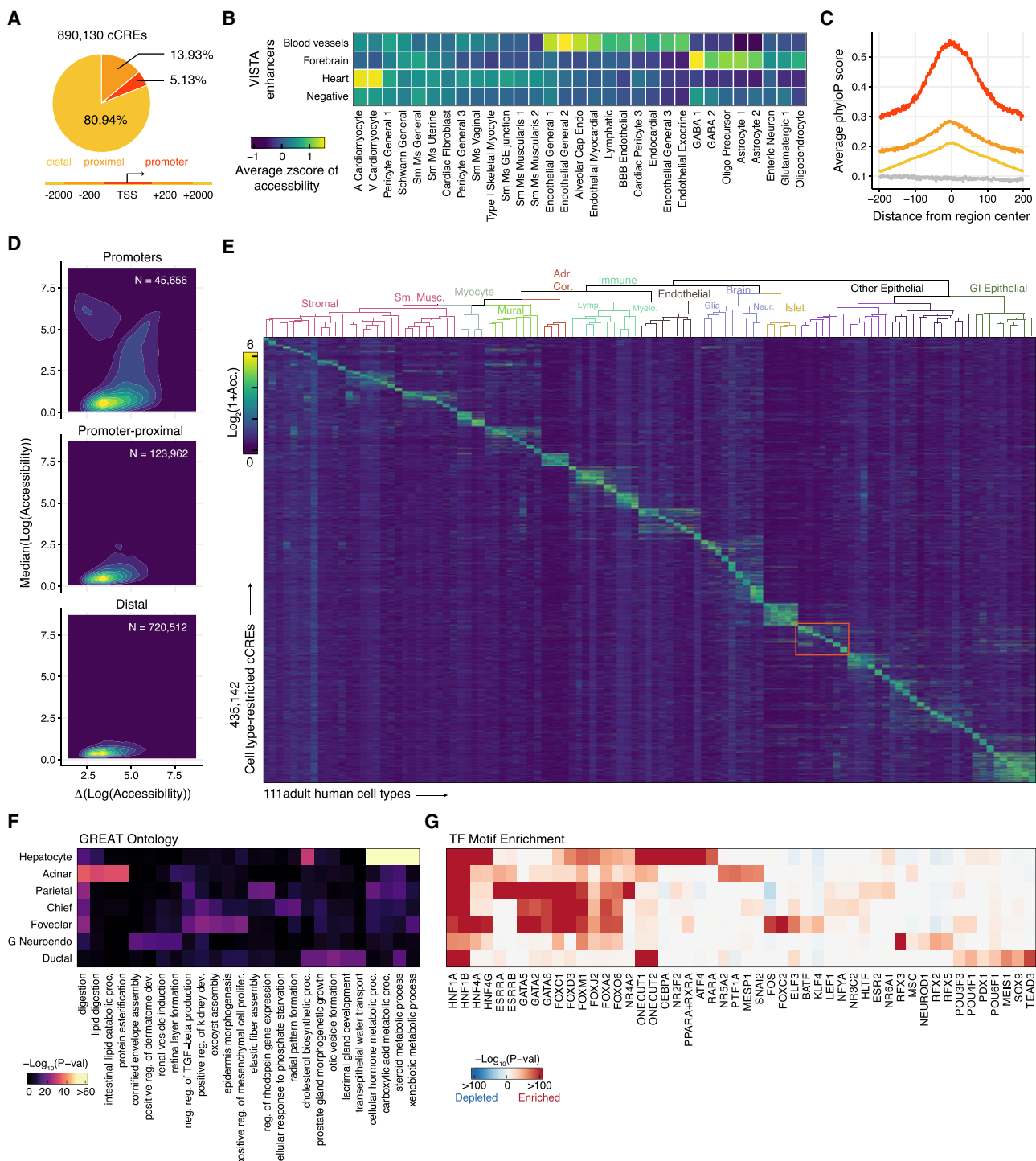


**Figure 2. An atlas of cCREs in adult human cell types**

- (A) Classification of 890,130 cCREs across the human genome based on their distances to annotated TSSs.
- (B) Heatmap showing the average chromatin accessibility for each of four groups (blood vessel, forebrain, heart, and negative control) of validated tissue-specific enhancers from the VISTA database (Visel et al., 2007) across indicated cell types. Z scores were calculated using all 111 cell types. The top 10 cell types in each validated enhancer group are shown.
- (C) Average phyloP (Pollard et al., 2010) conservation scores of cCREs stratified by groups defined in (A). Genomic background is indicated in gray.
- (D) Two-dimensional density plot showing the median chromatin accessibility compared with the range (difference between maximum and minimum) of chromatin accessibility across 111 cell clusters for 890,130 cCREs, stratified by groups defined in (A).

(legend continued on next page)

clustered based on cell type rather than tissue of origin or individual (Figure 1E). On the other hand, tissue-resident fibroblasts clustered into seven subtypes with diverse tissues of origin for each (Figure 1E). Notably, the majority of the 111 cell types exhibited high tissue specificity. For example, highly specialized cell types such as follicular cells, pneumocytes, and hepatocytes were restricted to only one tissue type, reflecting their tissue-specific functions (Figure 1E). Finally, we observed that the cell types we identified by sci-ATAC-seq are highly concordant with those identified by single-cell RNA sequencing (RNA-seq) experiments on corresponding tissues (Data S1).

### An atlas of cCREs in adult human cell types

To identify accessible chromatin regions in each of the 111 cell types, we aggregated chromatin accessibility profiles from all nuclei comprising each cell cluster and applied a peak calling procedure optimized for single-cell data (Methods S1; STAR Methods). We then merged these accessible chromatin regions to obtain a list of 890,130 non-overlapping cCREs (Figure 2A). These cCREs covered 58.9% of the elements in the registry of cCREs published by the ENCODE consortium (Moore et al., 2020) and also included 420,152 previously unannotated elements (Figure S1A). To benchmark these cCREs, we next compared chromatin accessibility profiles between biosamples profiled by bulk DNase-seq and cell types identified by sci-ATAC-seq in the current study. In aggregate, sci-ATAC-seq cell types resembled primary cell type biosamples more closely than bulk tissue or immortalized cell line biosamples (Figure S1B), and prevalent cell types with higher tissue abundance defined by sci-ATAC-seq showed closer similarities to bulk DNase-seq biosamples than rare cell types did (Figure S1C). Out of the 111 cell types profiled in the current study, 44 (40%) did not show statistically significant correlation with any bulk biosample profiled by the ENCODE consortium (Figure S1D). Many of these cell types were rare: their median maximal tissue abundance was only 3.2%, and 36 (81.8%) of them constituted fewer than 10% of all cells in any tissue. Taken together, these findings suggest that our dataset contributes previously underrepresented cCREs from *in vivo* human cell types to existing catalogs, particularly from cell types with low abundance in bulk tissues.

To assess the potential function of these cCREs, we next compared them with catalogs of transgenic reporter-validated mammalian enhancers (Visel et al., 2007) and found that validated tissue-specific enhancers exhibited much higher chromatin accessibility in cell types comprising a large proportion of nuclei identified in the corresponding tissue (Figure 2B). For example, validated enhancers in heart showed higher average chromatin accessibility in atrial cardiomyocytes ( $Z$  score: 1.41) and ventricular cardiomyocytes ( $Z$  score: 1.43) compared with other cell types (Figure 2B), suggesting a good correlation between cell-type-specific chromatin accessibility and tissue-specific enhancer activity. We further found that expression quantitative

trait loci (eQTLs) from 49 adult tissue types (GTEx Consortium, 2020) were most commonly accessible in prevalent cell types, such as endothelial and smooth muscle cells. In addition, eQTLs from homogeneous tissues, such as liver and thyroid, displayed strongest accessibility in the corresponding cell type which comprised a large proportion of nuclei identified in the tissue (Figures S2A and S2B). These results suggest that bulk tissue eQTLs best represent sequence variants associated with gene expression in abundant cell types and homogeneous tissues and may be less representative for rarer cell types within homogeneous tissues or for unique cell types from heterogeneous tissues.

We next categorized each cCRE based on distance to the nearest TSS as shown in Figure 2A. The majority (80.94%) of cCREs in the current catalog resided more than 2,000 bp away from annotated TSSs. cCREs located directly over TSSs or near promoter regions displayed higher levels of sequence conservation and elevated chromatin accessibility (Figures 2C and 2D). By contrast, gene-distal cCREs were less accessible and showed larger variance relative to their accessibility (Figure 2D), suggesting the presence of shared programs of highly accessible promoter-proximal cCREs alongside variable programs of gene-distal cCREs across cell types and species. To further dissect cell-type-specific chromatin signatures and regulatory programs, we applied an entropy-based strategy (Schug et al., 2005) to reveal 435,142 cCREs that demonstrated restricted accessibility in one or a few cell types (Figure 2E; STAR Methods). We next applied GREAT ontology enrichment analysis and motif enrichment analysis on cell-type restricted cCREs to reveal putative biological processes and TFs of each cell type, which largely correlated with expected cell-type-specific functions (false discovery rate [FDR] <0.01). For instance, cCREs restricted to hepatocytes yielded biological process ontology terms such as steroid metabolic process (Figure 2F) and were enriched for the binding sites of hepatocyte nuclear factor TF family members HNF1A/B, HNF4A/G, and ONECUT1/2 (Figure 2G) (Costa et al., 2003).

### Integrative analysis of adult and fetal chromatin accessibility

To examine transcriptional regulators and cCRE remodeling between fetal and adult stages, we re-processed data from a recent cell atlas of chromatin accessibility in 15 human fetal tissue types (Domcke et al., 2020) using the same quality control, clustering, and annotation strategies described above, which led to the discovery of 111 fetal cell types and 802,025 cCREs (Figure S3; Table S3). Combining these cCREs with those identified from the adult cell types, we mapped a total of 1,154,611 distinct cCREs spanning 14.8% of the human genome in 222 fetal and adult cell types (Mendeley Data: 10.17632/yv4fzv6cnm.1). These cCREs covered 58.5% and 69.7% of the elements in the EpiMap (Boix et al., 2021) and the ENCODE cCRE registry (Moore et al., 2020), respectively. In addition,

(E) Heatmap representation of 435,142 cCREs showing cell-type-restricted patterns in 111 cell types. Color represents  $\log_2$ -transformed chromatin accessibility. (F and G) Heatmaps showing Gene Ontology (GO) terms (F) and TF motifs (G) with maximal enrichment in cell-type-restricted cCREs of selected cell types. Only the most enriched TF motif in each of the previously identified motif archetypes (Vierstra et al., 2020) was selected as the representative and the top 10 motifs were selected for each cell type. Color represents  $-\log_{10}P$ . Full GO and motif enrichments are available on Mendeley Data (10.17632/yv4fzv6cnm.1). See also Figures S1 and S2 and Methods S1.

34.8% and 51.0% of our cCREs were not annotated by the Epi-Map and the ENCODE cCRE registry, respectively.

To compare the 222 fetal and adult cell types across the two atlases of chromatin accessibility, we utilized SnapATAC followed by batch-correction to obtain a low dimensional representation of the 1,323,041 nuclei from both fetal and adult tissues (Figures 3A and 3B; STAR Methods). We next performed phylogenetic analysis to place the fetal and adult cell types into different groups based on the distance defined in the low dimensional space (Figure S4A; STAR Methods). In general, cell types belonging to different lineages separated into independent groups and harbored specific cCREs that were enriched for previously characterized lineage-specific TF motifs (Figure S4B). However, although many fetal cell types such as lymphoid, myeloid, and endothelial cells clustered near their adult counterparts in the tree, some cell types such as neurons and skeletal myocytes, differed drastically between adult and fetal stages (Figure S4A), suggesting distinct cCRE usage by these cell types during development. To more systematically quantify differences in chromatin accessibility between adult and fetal cell types, we compared normalized accessibility across the list of 1,154,611 cCREs for each pair of fetal and adult cell types (Figures 3C, 3D, and S5). We found that fetal cell types, such as immune and endothelial cells, showed a relatively higher correlation with their adult counterparts than did other cell types such as neurons, glial cells, and skeletal myocytes (Figure 3D), consistent with the findings from our phylogenetic analysis. Together, these analyses suggest that the extent to which cCREs remodel to achieve developmental-stage specific functions varies greatly between human cell types.

To reveal the specific elements that may underlie fetal or adult-specific regulatory programs, we calculated life stage-specific cCREs for major cell groups that contained corresponding adult and fetal cell types (Figure 4A). Characterization of these elements revealed striking life stage-specific regulatory programs (Figures 4B and 4C). For example, skeletal myocytes differentiate substantially during pre- and post-natal development (Chal and Pourquié, 2017) and showed lower global similarity between life stages than most other major cell types (Figures 3C and 3D). In total, we identified 72,648 differentially accessible (DA) cCREs between fetal and adult skeletal myocytes (Figure 4D). DA cCREs in fetal myocytes were associated with biological processes such as embryo development and response to wounding and were enriched for motifs of myogenic regulatory TFs (MRFs) that orchestrate normal myogenesis (Pownall et al., 2002) (Figures 4E and 4F), highlighting the role of these elements in regulating myogenic properties of fetal myocytes. On the other hand, adult skeletal myocyte DA cCREs were associated with biological processes related to muscle adaptation to contractile activity as well as insulin and steroid hormone response and were enriched for MEF family members ( $p = 1e-424$ ) and AP-1 complex members including FOSL1 ( $p = 1e-274$ ) (Figures 4D and 4E), suggesting a role for these elements in regulating transcriptional responses to hormonal exposures and load bearing in adult skeletal muscle. In line with these ontology results and with established patterns of myosin isoform expression across the human lifespan (Schiaffino and Reggiani, 2011; Schiaffino

et al., 2015; Stuart et al., 2016), we discovered DA cCREs at loci encoding marker genes of pre-natal myocytes including *MYH3* and *MYH8*, the heavy chains of embryonic and neonatal myosin respectively, as well as markers of type I (slow) and type II (fast) twitch adult myocytes including *MYH6/MYH7* and *MYH1/MYH2*, respectively (Figure 4F). Taken together, these findings reveal the regulatory elements that may underlie the proliferative capacity and mature functionality of fetal and adult skeletal myocytes, respectively, and emphasize the value of this dataset alongside emerging human cell atlases collected at different time points along the lifespan for determining life stage-specific gene regulatory programs at cell-type resolution.

#### Delineation of cell-type specificity of human cCREs

To characterize the cell-type specificity of cCREs across fetal and adult cell types, we organized the 1,154,611 cCREs into 150 clusters, referred to as *cis*-regulatory modules (CRMs), based on their normalized accessibility across the 222 cell types. Although several CRMs displayed shared accessibility patterns across all cell types, most CRMs were limited either to single fetal or adult cell types or to groups of cell types that reflected shared cellular lineages (Figure 5A). To annotate putative functions of CRMs, we applied GREAT ontology enrichment analysis (McLean et al., 2010). Broadly, CRMs showing preferential accessibility in specific fetal and adult cell types were enriched for biological process ontology terms related to both cell type and life stage-specific cellular processes (FDR <0.01) (Figures 5B and 5C).

To identify sequence features underlying these CRMs, we next measured the enrichment of 1,565 human TF motifs across the 150 CRMs to reveal putative master regulators of fetal and adult human cell types. This analysis revealed a comprehensive catalog of fetal and adult cell and lineage-specific TF motifs. For example, a module with strong accessibility in adult CD8<sup>+</sup> T cells and natural killer T cells was distinguished by enrichment for TBR, EOMES, and TBX TF family motifs (module 8,  $p < 1e-84$ ) (Figures 5B–5D), modules with strong accessibility in B cells were distinguished by enrichment for EBF family TF motifs (module 13,  $p = 1e-27$ ; module 17,  $p = 1e-197$ ), and a module with strong accessibility in adult mast cells was distinguished by GATA family member motif enrichment (module 25,  $p = 1e-84$ ) (Figures 5B–5D). Further, the module with the strongest accessibility across all identified cell types was characterized by enrichment of the SP1 motif (module 1,  $p = 1e-9180$ ), consistent with the original description of SP1 as a regulator of ubiquitously expressed housekeeping genes (Black et al., 2001). In addition to these well-characterized associations, we also report previously undefined TF associations with human cell types that are challenging to study in their *in vivo* tissue contexts: for example, motifs of the ESRR (module 92,  $p = 1e-357$ ; module 93,  $p = 0.1$ ) and FOX (module 92,  $p = 1e-36$ ; module 93,  $p = 1e-255$ ) TF family were preferably enriched in modules accessible in fetal (module 92) and adult (module 93) gastric epithelial cells, respectively (Figure 5A), and motifs of the FOS and JUN families were enriched in modules accessible in fetal and adult adrenal cortical cells (modules 135–138,  $p < 1e-10$ ; Figure 5A).

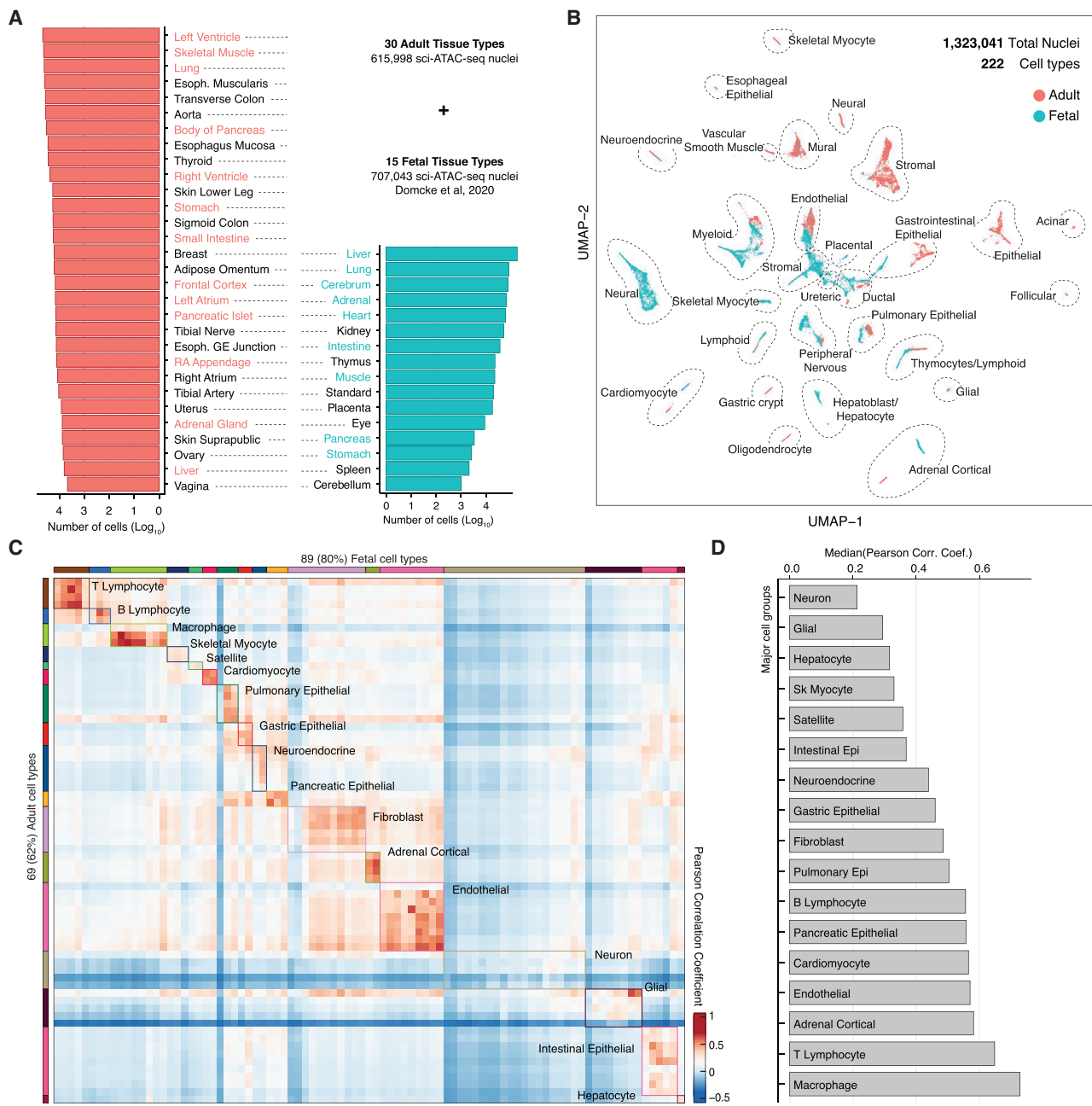


**Figure 3. Integrative analysis of adult and fetal single-cell chromatin accessibility atlases**

(A) Number of sci-ATAC-seq cells per tissue type for 30 adult and 15 human fetal tissue types that were integrated. Matching tissue types between adult and fetal datasets are highlighted in red or blue respectively. Standard, sentinel tissue (trisomy 18 cerebrum).

(B) UMAP embedding of 1,323,041 nuclei from fetal and adult tissues. Each dot in the scatterplot represents a nucleus, colored by life stage.

(C) Heatmap showing Pearson correlation coefficient (PCC) between 69 adult cell types and 89 fetal cell types from 17 manually defined cell groups that are present in both adult and fetal tissues. A comprehensive heatmap is provided in Figure S5.

(D) Bar plot showing the median PCC for each major cell group indicated in (C).

See also Figures S3 and S4.

### Association of human cell types with complex traits and diseases

We next sought to use our 1.2 million cell-type-resolved cCREs to interpret genetic variants associated with complex traits and

multigenic disease phenotypes. We downloaded the NHGRI-EBI GWAS catalog (Bunielo et al., 2019) and retained 1,123 well-powered GWAS with 10 or more significant SNPs and over 20,000 cases (14% of 8,219 GWAS publications). We then

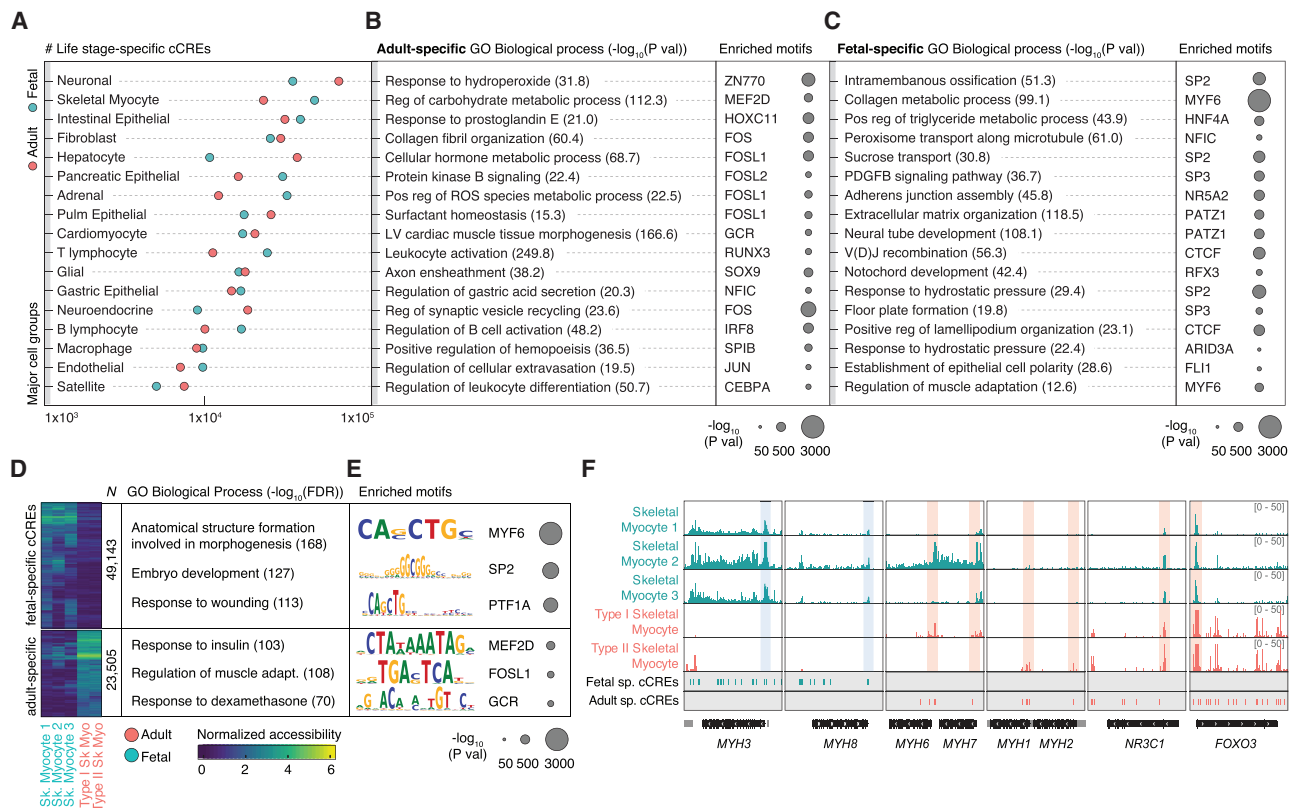


**Figure 4. Differential chromatin accessibility landscapes in adult and fetal human cell types**

- (A) Dot plot showing the number of adult and fetal specific cCREs detected for each major cell group indicated in (C).
- (B and C) Significant GO biological process ontology terms and transcription factor motif enrichments for adult-specific (B) and fetal-specific (C) cCREs.
- (D) Heatmap representation of 72,648 differentially accessible (DA) cCREs between fetal and adult skeletal myocytes along with significant GREAT biological process ontology enrichments (McLean et al., 2010). Color represents log-transformed normalized signal.
- (E) Significantly enriched TF motifs within fetal and adult skeletal myocyte DA cCREs. The most enriched motif within each motif archetype (Vierstra et al., 2020) was selected and the top three were displayed.
- (F) Genome browser tracks showing chromatin accessibility for fetal and adult skeletal myocytes along with DA cCREs between the adult and fetal skeletal myocytes. Indicated genes are shown in black, other genes are shown in gray. TSSs of the indicated genes are shaded in red and blue.

used a hypergeometric test to measure the enrichment of trait-associated variants within cCREs identified from the 222 fetal and adult cell types. GWAS variants of 450 traits/diseases were found to be enriched in cCREs from at least one cell type (FDR <0.1%) (Figure S6). As a comparison, EpiMap, a comprehensive enhancer catalog comprising 833 epigenomic maps from bulk human tissue samples, primary cells, and ex vivo cell lines (Boix et al., 2021), captured 457 GWAS studies (FDR <0.1%) (Figure S6). For the 290 traits shared by both this study and EpiMap, our data captured the strongest GWAS enrichment in 74.8% of cases (217 of 290) and provided improved resolution by linking complex traits to specific cell type(s) (Figure S6). Further, for 160 additional traits, we were able to identify enrichments that were not detected in previous analyses (Figure S6), highlighting the added value of cell-type-resolved cCREs maps.

The GWAS enrichment analysis above considered only index variants (i.e., SNPs in genome-wide significant loci). However, the index variants may not represent the specific causal variants due to linkage disequilibrium (Schaid et al., 2018) and much of

the heritability lies in SNPs with associations that do not reach genome-wide significance (Yang et al., 2010). We thus curated 240 GWAS studies with publicly available summary statistics and examined the enrichment of their associated SNPs within cCREs annotated in fetal and adult cell types using stratified linkage disequilibrium score regression (LDSC), a method for identifying functional enrichment from GWAS summary statistics using genome-wide information from all SNPs and explicitly modeling linkage disequilibrium (Finucane et al., 2015). This analysis revealed a total of 3,220 significant (FDR <0.1) associations between fetal and adult cell types and human traits and disease phenotypes (Figure 6; Table S4). These enrichments revealed many expected cell-type-disease phenotype relationships—for example, eczema risk variants were strongly enriched in adult T lymphocyte cCREs, atrial fibrillation risk variants were strongly enriched in both adult and fetal atrial and ventricular cardiomyocyte cCREs (FDR <0.001), and thyroid stimulating hormone variants were enriched in follicular cell cCREs (Figure 6; Table S4). In addition to expected relationships, our analysis

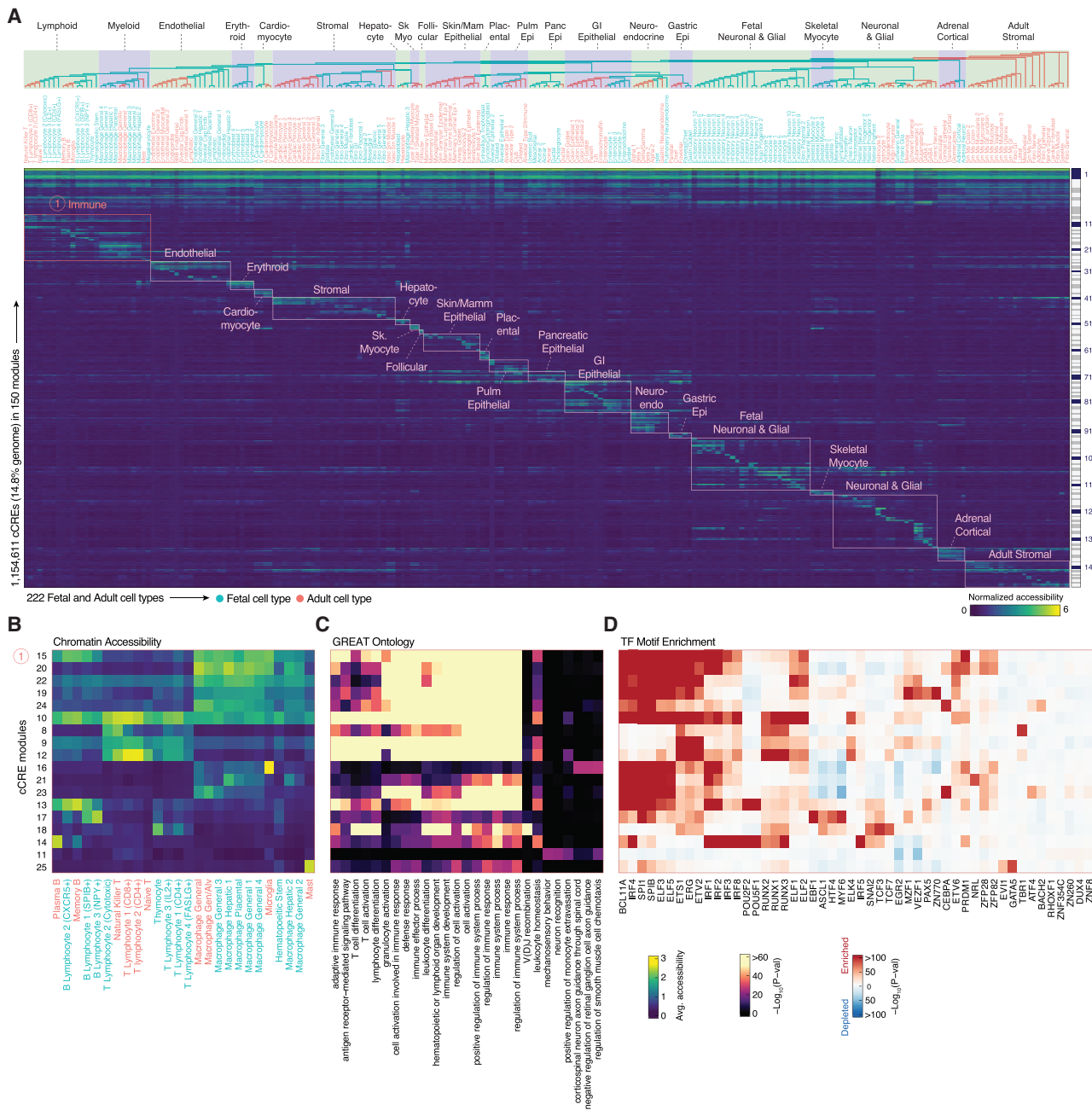


**Figure 5. Delineation of CRE modules across 222 fetal and adult human cell types**

(A) Heatmap representation of chromatin accessibility for 1,154,611 cCREs across 222 fetal and adult cell types. Color represents normalized chromatin accessibility. cCREs were organized into 150 modules by K-means clustering, indicated by the color bars on the right. 20 groups of lineage-specific modules (colored boxes) are highlighted.

(B–D) Heatmaps showing chromatin accessibility (B), GO terms (C), and motifs (D) with maximal enrichment in a subset of CRE modules (rows) for immune cell types. The GO and motif heatmaps are colored by enrichment  $-\log_{10}P$ . Only the most enriched TF motif in each of the previously identified motif archetypes ([Vierstra et al., 2020](#)) was selected as the representative and the top 5 motifs were selected for each module. Full GO and motif enrichments are available on Mendeley Data (10.17632/yv4fzv6cnm1).

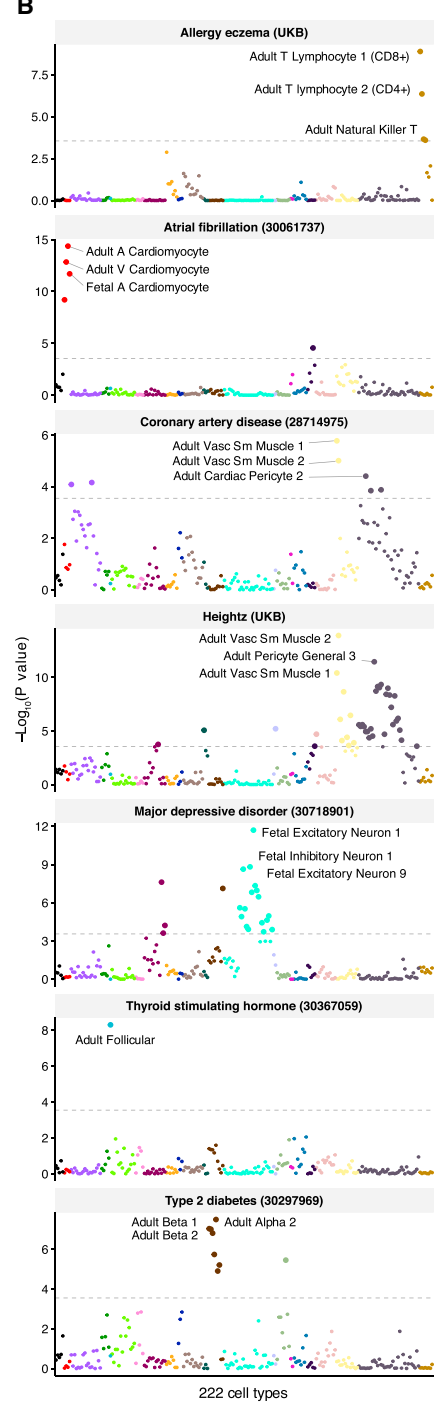
also revealed GWAS enrichment for human cell types not presently annotated by bulk DNase-seq or ATAC-seq data. These included a strong enrichment of coronary artery disease variants in adult vascular smooth muscle cCREs ( $FDR < 0.001$ )

in addition to fetal and adult fibroblast, pericyte, and endothelial cell cCREs (FDR <0.01), COPD variants in several adult stromal smooth muscle cell types (FDR <0.01), triglyceride and HDL cholesterol level-associated variants in adult adipocyte cCREs

**A**



**B**



(legend on next page)

(FDR <0.01), and a nominal enrichment of ulcerative colitis variants in colon epithelial cell cCREs ( $p < 0.02$ ). Interestingly, we detected substantial differences in the enrichment of disease and trait-associated noncoding variants in subtypes of adult and fetal fibroblasts. These included a significant enrichment of variants associated with birth weight in fetal fibroblasts (FDR <0.01) but not in adult fibroblasts (Table S4). Further, we detected differences in the enrichment of disease and trait variants in subtypes of adult fibroblasts, each of which displayed unique regulatory elements in addition to comparable chromatin accessibility at a set of core fibroblast cCREs (Figure S7). Although all adult fibroblast populations were enriched for variants associated with standing height to an equivalent degree (FDR <0.001), adult epithelial fibroblasts displayed a striking enrichment for variants associated with balding (FDR <0.001) and only adult cardiac fibroblasts showed any enrichment for variants associated with myocardial fractal dimensions (FDR <0.1) (Table S4).

#### Systematic interpretation of molecular functions for noncoding risk variants

Many noncoding genetic variants enriched within cCREs from the analysis above are hypothesized to alter the expression of disease-associated genes by disrupting TF binding to *cis*-regulatory elements (Claussnitzer et al., 2020). To systematically interpret molecular mechanisms for the specific genetic variants associated with complex traits, we first applied the activity-by-contact (ABC) model (Fulco et al., 2019) to link the cCREs identified in 111 adult cell types to their target genes using our previously published promoter capture Hi-C data from 15 adult human tissues (Jung et al., 2019) (STAR Methods). This analysis revealed 5,723,307 unique distal cCRE-to-gene linkages across the 111 adult cell types, with a median of 726,514 total linkages and 6,804 cell-type-specific linkages per cell type (Figure S8). Second, we determined the probability that variants from 48 GWAS were causal for disease or trait association (posterior probability of association [PPA]) using Bayesian fine-mapping (Wakefield, 2009). We defined likely causal variants as those with a PPA >0.1 and found that they were more likely to reside within cCREs than variants with low PPA (Figure S8A). Overall, we detected 3,096 likely causal variants residing within cCREs mapped in 111 adult human cell types (Figures 7A and 7B; Table S5), 2,096 of which were linked to putative target genes via the ABC model (Figure 7A; Table S5). Third, we applied our recently developed deltaSVM models for 94 TFs (Yan et al., 2021) to identify variants potentially disrupting binding by these regulators. This analysis revealed 527 TF binding sites predicted to be significantly altered by the likely causal variants (Figure 7A;

Table S5). The intersection of these lists prioritized 361 likely causal variants that (1) resided within a human cell type cCRE, (2) significantly altered TF binding, and (3) were linked to one or more target genes (Figures 7A and 7B; Table S5).

For example, one likely causal variant for ulcerative colitis (rs16940186) resided within an intergenic cCRE restricted to epithelial cells of the gastrointestinal tract, particularly colon epithelial cells, enterocytes, and goblet cells (Figure 7C). The cCRE containing rs16940186 was predicted to contact the TSS of *IRF8* (ABC score >0.015), which encodes a TF involved in the regulation of immune cell maturation (Salem et al., 2020) and regulation of innate immunity in gastric epithelial cells (Yan et al., 2016). The rs16940186 risk allele is an eQTL associated with increased *IRF8* expression in human colon tissue and, consistent with these findings, deltaSVM models predicted this risk allele to create a binding site for the ETS family of activating TFs (Figure 7C), which are expressed in intestinal epithelia and have been suggested to regulate intestinal epithelial maturation (Jedlicka et al., 2009). One other prioritized likely causal risk variant for osteoarthritis (rs75621460) resided within a cCRE that was primarily accessible in immune cell types, was predicted to target the immunosuppressive cytokine gene *TGFB1*, and disrupted a binding site for the zinc-finger TF ERG1 (Figure 7D).

#### DISCUSSION

Detailed knowledge of the regulatory programs that govern gene expression in the human body has key implications for understanding human development and disease pathogenesis. Here, we used single-cell ATAC-seq to profile chromatin accessibility in 615,998 cells across 30 adult human tissues representing a wide range of human organ systems and integrated this dataset with single-cell chromatin accessibility data from human fetal tissues (Domcke et al., 2020). We mapped the state of activity for ~1.2 million cCREs across 222 fetal and adult cell types, bridging the key gap of cell type resolution in the annotation of candidate regulatory elements in the human genome. This work highlights the value of integrating human sci-ATAC-seq datasets from multiple sources and time points (Chiou et al., 2021; Domcke et al., 2020; Hocker et al., 2021; Wang et al., 2020) and, in the future, integration of these data along with new human single-cell datasets of increasing scale, breadth, and depth will enable a comprehensive understanding of gene regulatory features of human cell types throughout the lifespan.

Although genome-wide association studies (GWAS) have been broadly used to enhance our understanding of polygenic

**Figure 6. Association of fetal and adult human cell types with complex traits and diseases**

(A) Heatmap showing enrichment of risk variants associated with disease and non-disease traits from genome-wide association studies in human cell-type-resolved cCREs. Cell-type-stratified linkage disequilibrium score regression (LDSC) analysis was performed using GWAS summary statistics for 240 phenotypes. Total cCREs identified independently from each fetal and adult cell type were used as input for analysis.  $p$  values were corrected using the Benjamini-Hochberg procedure for multiple tests. FDRs of LDSC coefficient are displayed. 66 selected traits were highlighted on the left, with PubMed identifiers (PMIDs) or "UKB," indicating summary statistics downloaded from the UK Biobank, enclosed in parentheses. Numerical results are reported in Table S4.

(B) Dot plots showing significance of enrichment for selected traits from (A) within cCREs from 222 fetal and adult cell types. Each circle represents a cell type. Large circles pass the cutoff of FDR <1% at  $-\log_{10}(P) = 3.55$ . The top 3 most highly associated cell types are labeled for each trait. Comprehensive data are provided in Table S4.

See also Figures S6 and S7 and Table S5.

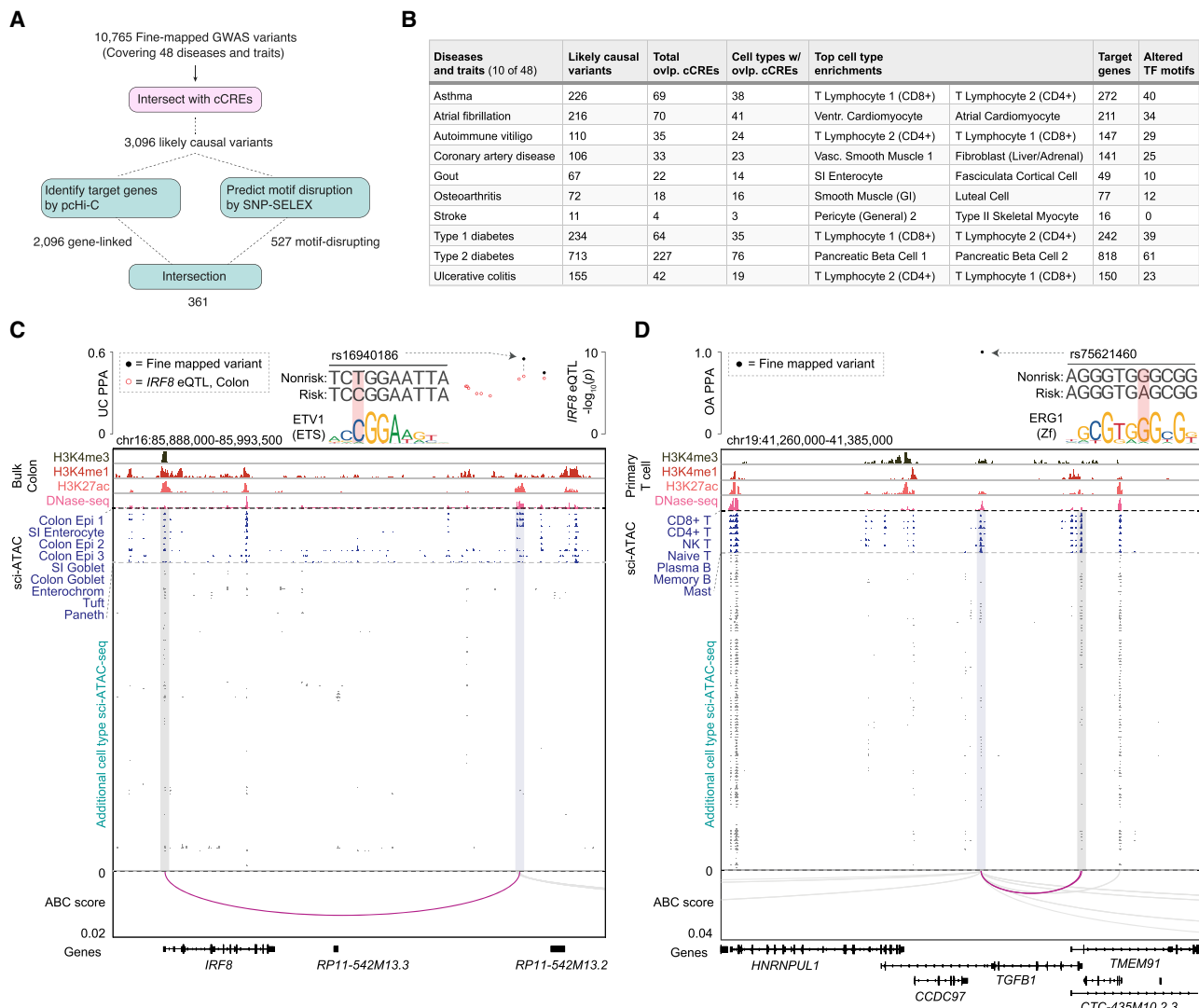


**Figure 7. Systematic interpretation of molecular functions of noncoding risk variants**

(A) Schematic illustrating the workflow for annotating fine-mapped noncoding risk variants.  
(B) Table showing the number of likely causal variants (PPA >0.1), number of cCREs overlapping likely causal variants, number of cell types in which overlapping cCREs are accessible, top cell types variants are enriched in based on LD score regression (Bulik-Sullivan et al., 2015), number of predicted target genes for likely causal variants, and significantly altered motifs predicted by deltaSVM model trained using SNP-SELEX data for 10 examples out of 48 total fine-mapped diseases and traits. Comprehensive data are provided in Table S5.

(C and D) Fine mapping and molecular characterization of an ulcerative colitis (UC) risk variant (C) in a gastrointestinal (GI) epithelial cell cCRE and an osteoarthritis variant (D) in an immune cell cCRE. Genome browser tracks (GRCh38) display chromatin immunoprecipitation sequencing (ChIP-seq) and DNase-seq from ENCODE human colon datasets (C) and primary T cell datasets (D) as well as chromatin accessibility profiles for cell types from sci-ATAC-seq. Chromatin interaction tracks show linkages between the variant-containing cCREs and genes from promoter capture Hi-C data via activity-by-contact (ABC) (Fulco et al., 2019) analysis. All linkages shown have an ABC score >0.015. PPA, posterior probability of association.

See also Figure S8.

human traits and reveal clinically relevant therapeutic targets for complex diseases, to date the discovery of new variants has far outpaced our ability to interpret their molecular functions (Claussnitzer et al., 2020). Two central goals of the current study were thus to link individual human cell types to complex traits and to leverage cCRE maps to interpret the molecular functions of specific noncoding risk variants. By applying our datasets alongside cutting-edge methods to prioritize likely causal vari-

ants in LD, link distal cCREs to putative target genes, and predict motifs altered by risk variants, we revealed thousands of cell-type-trait associations and created a framework to systematically interpret noncoding risk variants. For example, we highlight the likely causal ulcerative colitis-associated variant rs16940186. This risk variant may function to increase *IRF8* expression in gastrointestinal epithelial cells by creating a binding site for ETS family TFs in a GI epithelial-specific enhancer,

and thereby alter the transcriptional responses of intestinal epithelial cells to inflammatory cytokines. Pending functional validation experiments, our results suggest that targeting *IRF8* in GI epithelial cells could be a potential therapeutic target for ulcerative colitis. As future GWAS in large cohorts with detailed phenotyping, whole genome sequencing efforts, and additional association studies employing long read technologies to capture structural variants become available, we anticipate that this combined resource and framework will be of continued utility for the interpretation of molecular functions for noncoding genetic variants. This resource thus lays the foundation for the analysis of gene regulatory programs across human organ systems at cell-type resolution and accelerates the interpretation of non-coding sequence variants associated with complex human diseases and phenotypes. The datasets can be accessed and explored at <http://catlas.org/humanenhancer>.

### Limitations of study

The current study is still limited in several ways: first, we solely integrated data from two discrete life stages and in an incomplete sampling of organ systems. Although we utilized tissue from anatomic sites corresponding directly to existing biosamples in large-scale databases (Carithers et al., 2015; Stranger et al., 2017), the size and diversity of adult human organ systems make it difficult to representatively sample them in their entirety. Additionally, our assay solely profiles chromatin accessibility in dissociated nuclei, and thus misses key orthogonal molecular and spatial information. Future assays that incorporate gene expression, chromatin accessibility, histone modifications, DNA methylation, chromosomal conformation, TF binding, and spatial information in the same single-cell will greatly enhance our understanding of gene regulation in human cell types (Zhu et al., 2020).

### STAR★METHODS

Detailed methods are provided in the online version of this paper and include the following:

- [KEY RESOURCES TABLE](#)
- [RESOURCE AVAILABILITY](#)
  - Lead contact
  - Materials availability
  - Data and code availability
- [EXPERIMENTAL MODEL AND SUBJECT DETAILS](#)
  - Human Subjects
- [METHOD DETAILS](#)
  - Tissue feasibility testing for sci-ATAC-seq
  - Combinatorial indexing-assisted single nucleus ATAC-seq
  - Demultiplexing of single nucleus ATAC-seq sequencing reads
  - Quality control metrics: TSS enrichment and unique fragments
  - Overall clustering strategy
  - Doublet removal
  - Dimension reduction
  - Correction of Batch Effects

- Graph-based clustering algorithm
  - Peak calling and peak filtering
  - Generating the union peak set
  - Computing relative accessibility scores
  - Assigning cell types to cell clusters
  - Identification of cell type-restricted peaks
  - Cell-type enrichment analysis of fine-mapped GTEx eQTLs
  - Differential peak analysis
  - Identification of fibroblast core signature and subtype-specific signatures
  - Measuring the similarity of chromatin accessibility profiles between cell types identified by sci-ATAC-seq and bulk biosamples
  - Identification of cCRE modules
  - Motif enrichment analysis
  - Identification of candidate driver TFs
  - Integration of adult and fetal datasets
  - Differential peak analysis between fetal and adult cells
  - Generation of bigwig tracks
  - Linking cCREs to target genes
  - Stratified linkage disequilibrium (LD) score regression
  - GWAS enrichment analysis
  - Fine mapping
  - Predicting the effects of noncoding variants on TF binding
  - External genome browser track data
- [QUANTIFICATION AND STATISTICAL ANALYSIS](#)
  - [ADDITIONAL RESOURCES](#)

### SUPPLEMENTAL INFORMATION

Supplemental information can be found online at <https://doi.org/10.1016/j.cell.2021.10.024>.

### ACKNOWLEDGMENTS

We thank the ENCODE consortium, in particular Mike Pazin (NHGRI), Idan Gadbck (Stanford), Kristin Ardlie (Broad Institute), and Ellen Gelfand (Broad Institute), for providing the human tissue samples for the present study. We thank B. Li for bioinformatics support. We thank S. Kuan for sequencing support. We thank B. Chen for valuable discussion and feedback in earlier versions of the manuscript. We thank the QB3 Macrolab at UC Berkeley for purification of the Tn5 transposase. This work was supported by the Ludwig Institute for Cancer Research (to B.R.), National Human Genome Research Institute (3U54HG006997-04S2 to B.R.), and Foundation for the NIH (AMP T2D RFP 14 to K.J.G.). J.D.H. was supported in part by a Ruth L. Kirschstein Institutional National Research Service Award T32 GM008666 from the National Institute of General Medical Sciences. Work at the UCSD Center for Epigenomics was supported by the UC San Diego School of Medicine.

### AUTHOR CONTRIBUTIONS

Conceptualization, J.D.H., S.P., A.W., and B.R.; Study Supervision, B.R.; Supervision of Data Generation, S.P., A.W., and B.R.; Contribution to Data Generation, J.D.H., X.H., and M.M.; Contribution to Data Analysis: K.Z., J.D.H., J.C., O.P., Y.E.L., and Y.Q.; Contribution to Web Portal, Y.E.L. and K.Z.; Contribution to Data Interpretation, K.Z., J.D.H., S.P., A.W., and K.J.G.; Contribution to Writing the Manuscript, K.Z., J.D.H., and B.R. All authors edited and approved the manuscript.

## DECLARATION OF INTERESTS

B.R. is a shareholder and consultant of Arima Genomics, Inc., and a co-founder of Epigenome Technologies, Inc. K.J.G. is a consultant of Genentech and a shareholder in Vertex Pharmaceuticals. These relationships have been disclosed to and approved by the UCSD Independent Review Committee.

Received: January 27, 2021

Revised: July 30, 2021

Accepted: October 21, 2021

Published: November 12, 2021

## SUPPORTING CITATIONS

Chen et al., 2019; Litviñuková et al., 2020.

## REFERENCES

- Andersson, R., Gebhard, C., Miguel-Escalada, I., Hoof, I., Bornholdt, J., Boyd, M., Chen, Y., Zhao, X., Schmidl, C., Suzuki, T., et al. (2014). An atlas of active enhancers across human cell types and tissues. *Nature* 507, 455–461.
- Astle, W.J., Elding, H., Jiang, T., Allen, D., Ruklisa, D., Mann, A.L., Mead, D., Bouman, H., Riveros-Mckay, F., Kostadima, M.A., et al. (2016). The Allelic Landscape of Human Blood Cell Trait Variation and Links to Common Complex Disease. *Cell* 167, 1415–1429.e19.
- Auton, A., Brooks, L.D., Durbin, R.M., Garrison, E.P., Kang, H.M., Korbel, J.O., Marchini, J.L., McCarthy, S., McVean, G.A., and Abecasis, G.R.; 1000 Genomes Project Consortium (2015). A global reference for human genetic variation. *Nature* 526, 68–74.
- Bentham, J., Morris, D.L., Graham, D.S.C., Pinder, C.L., Tombleson, P., Behrens, T.W., Martin, J., Fairfax, B.P., Knight, J.C., Chen, L., et al. (2015). Genetic association analyses implicate aberrant regulation of innate and adaptive immunity genes in the pathogenesis of systemic lupus erythematosus. *Nat. Genet.* 47, 1457–1464.
- Black, A.R., Black, J.D., and Azizkhan-Clifford, J. (2001). Sp1 and krüppel-like factor family of transcription factors in cell growth regulation and cancer. *J. Cell. Physiol.* 188, 143–160.
- Boix, C.A., James, B.T., Park, Y.P., Meuleman, W., and Kellis, M. (2021). Regulatory genomic circuitry of human disease loci by integrative epigenomics. *Nature* 590, 300–307.
- Bouneffouf, D., and Birol, I. (2016). Theoretical analysis of the minimum sum of squared similarities sampling for Nyström-based spectral clustering. In 2016 International Joint Conference on Neural Networks (IJCNN), pp. 3856–3862. <https://doi.org/10.1109/IJCNN.2016.7727698>.
- Bronson, P.G., Chang, D., Bhangale, T., Seldin, M.F., Ortmann, W., Ferreira, R.C., Urcelay, E., Pereira, L.F., Martin, J., Plebani, A., et al. (2016). Common variants at PVT1, ATG13-AMBRA1, AHI1 and CLEC16A are associated with selective IgA deficiency. *Nat. Genet.* 48, 1425–1429.
- Buenrostro, J.D., Giresi, P.G., Zaba, L.C., Chang, H.Y., and Greenleaf, W.J. (2013). Transposition of native chromatin for fast and sensitive epigenomic profiling of open chromatin, DNA-binding proteins and nucleosome position. *Nat. Methods* 10, 1213–1218.
- Bulik-Sullivan, B.K., Loh, P.-R., Finucane, H.K., Ripke, S., Yang, J., Patterson, N., Daly, M.J., Price, A.L., and Neale, B.M.; Schizophrenia Working Group of the Psychiatric Genomics Consortium (2015). LD Score regression distinguishes confounding from polygenicity in genome-wide association studies. *Nat. Genet.* 47, 291–295.
- Bunielo, A., MacArthur, J.A.L., Cerezo, M., Harris, L.W., Hayhurst, J., Malangone, C., McMahon, A., Morales, J., Mountjoy, E., Sollis, E., et al. (2019). The NHGRI-EBI GWAS Catalog of published genome-wide association studies, targeted arrays and summary statistics 2019. *Nucleic Acids Res.* 47 (D1), D1005–D1012.
- Carithers, L.J., Ardlie, K., Barcus, M., Branton, P.A., Britton, A., Buia, S.A., Compton, C.C., DeLuca, D.S., Peter-Demchok, J., Gelfand, E.T., et al.; GTEx Consortium (2015). A Novel Approach to High-Quality Postmortem Tissue Procurement: The GTEx Project. *Biopreserv. Biobank.* 13, 311–319.
- Carter, B., and Zhao, K. (2021). The epigenetic basis of cellular heterogeneity. *Nat. Rev. Genet.* 22, 235–250.
- Chal, J., and Pourquié, O. (2017). Making muscle: skeletal myogenesis *in vivo* and *in vitro*. *Development* 144, 2104–2122.
- Chen, H., Lareau, C., Andreani, T., Vinyard, M.E., Garcia, S.P., Clement, K., Andrade-Navarro, M.A., Buenrostro, J.D., and Pinello, L. (2019). Assessment of computational methods for the analysis of single-cell ATAC-seq data. *Genome Biol.* 20, 241.
- Chiou, J., Zeng, C., Cheng, Z., Han, J.Y., Schlichting, M., Huang, S., Wang, J., Sui, Y., Deogaygay, A., Okino, M.-L., et al. (2021). Single-cell chromatin accessibility identifies pancreatic islet cell type- and state-specific regulatory programs of diabetes risk. *Nat. Genet.* 53, 455–466.
- Claussnitzer, M., Cho, J.H., Collins, R., Cox, N.J., Dermitzakis, E.T., Hurles, M.E., Kathiresan, S., Kenny, E.E., Lindgren, C.M., MacArthur, D.G., et al. (2020). A brief history of human disease genetics. *Nature* 577, 179–189.
- Corces, M.R., Shcherbina, A., Kundu, S., Gloudemans, M.J., Frézard, L., Granja, J.M., Louie, B.H., Eulalio, T., Shams, S., Bagdatlı, S.T., et al. (2020). Single-cell epigenomic analyses implicate candidate causal variants at inherited risk loci for Alzheimer's and Parkinson's diseases. *Nat. Genet.* 52, 1158–1168.
- Cordell, H.J., Han, Y., Mells, G.F., Li, Y., Hirschfield, G.M., Greene, C.S., Xie, G., Juran, B.D., Zhu, D., Qian, D.C., et al.; Canadian-US PBC Consortium; Italian PBC Genetics Study Group; UK-PBC Consortium (2015). International genome-wide meta-analysis identifies new primary biliary cirrhosis risk loci and targetable pathogenic pathways. *Nat. Commun.* 6, 8019.
- Costa, R.H., Kalinichenko, V.V., Holterman, A.X., and Wang, X. (2003). Transcription factors in liver development, differentiation, and regeneration. *Hepatology* 38, 1331–1347.
- Cusanovich, D.A., Daza, R., Adey, A., Pliner, H.A., Christiansen, L., Gunderson, K.L., Steemers, F.J., Trapnell, C., and Shendure, J. (2015). Multiplex single cell profiling of chromatin accessibility by combinatorial cellular indexing. *Science* 348, 910–914.
- Cusanovich, D.A., Hill, A.J., Aghamirzaie, D., Daza, R.M., Pliner, H.A., Berleth, J.B., Filippova, G.N., Huang, X., Christiansen, L., DeWitt, W.S., et al. (2018). A Single-Cell Atlas of In Vivo Mammalian Chromatin Accessibility. *Cell* 174, 1309–1324.e18.
- Danecek, P., Bonfield, J.K., Liddle, J., Marshall, J., Ohan, V., Pollard, M.O., Whittham, A., Keane, T., McCarthy, S.A., Davies, R.M., and Li, H. (2021). Twelve years of SAMtools and BCFtools. *Gigascience* 10, giab008.
- Domcke, S., Hill, A.J., Daza, R.M., Cao, J., O'Day, D.R., Pliner, H.A., Aldinger, K.A., Pokholok, D., Zhang, F., Milbank, J.H., et al. (2020). A human cell atlas of fetal chromatin accessibility. *Science* 370, eaba7612.
- Ernst, J., Kheradpour, P., Mikkelsen, T.S., Shores, N., Ward, L.D., Epstein, C.B., Zhang, X., Wang, L., Issner, R., Coyne, M., et al. (2011). Mapping and analysis of chromatin state dynamics in nine human cell types. *Nature* 473, 43–49.
- Fang, R., Preissl, S., Li, Y., Hou, X., Lucero, J., Wang, X., Motamedi, A., Shiau, A.K., Zhou, X., Xie, F., et al. (2021). Comprehensive analysis of single cell ATAC-seq data with SnapATAC. *Nat. Commun.* 12, 1337.
- Finucane, H.K., Bulik-Sullivan, B., Gusev, A., Trynka, G., Reshef, Y., Loh, P.R., Anttila, V., Xu, H., Zang, C., Farh, K., et al.; ReproGen Consortium; Schizophrenia Working Group of the Psychiatric Genomics Consortium; RACI Consortium (2015). Partitioning heritability by functional annotation using genome-wide association summary statistics. *Nat. Genet.* 47, 1228–1235.
- Frankish, A., Diekhans, M., Ferreira, A.M., Johnson, R., Jungreis, I., Loveland, J., Mudge, J.M., Sisu, C., Wright, J., Armstrong, J., et al. (2019). GENCODE reference annotation for the human and mouse genomes. *Nucleic Acids Res.* 47 (D1), D766–D773.
- Franzén, O., Gan, L.-M., and Björkegren, J.L.M. (2019). PanglaoDB: a web server for exploration of mouse and human single-cell RNA sequencing data. *Database (Oxford)* 2019, 46.

- Fulco, C.P., Nasser, J., Jones, T.R., Munson, G., Bergman, D.T., Subramanian, V., Grossman, S.R., Anyoha, R., Patwardhan, T.A., Nguyen, T.H., et al. (2019). Activity-by-contact model of enhancer-promoter regulation from thousands of CRISPR perturbations. *Nat. Genet.* 51, 1664–1669.
- Furtado, M.B., Costa, M.W., Pranoto, E.A., Salimova, E., Pinto, A.R., Lam, N.T., Park, A., Snider, P., Chandran, A., Harvey, R.P., et al. (2014). Cardiogenic genes expressed in cardiac fibroblasts contribute to heart development and repair. *Circ. Res.* 114, 1422–1434.
- Grosselin, K., Durand, A., Marsolier, J., Poitou, A., Marangoni, E., Nemati, F., Dahmani, A., Lameiras, S., Reyal, F., Frey, O., et al. (2019). High-throughput single-cell ChIP-seq identifies heterogeneity of chromatin states in breast cancer. *Nat. Genet.* 51, 1060–1066.
- GTEx Consortium (2020). The GTEx Consortium atlas of genetic regulatory effects across human tissues. *Science* 369, 1318–1330.
- Guindon, S., and Gascuel, O. (2003). A simple, fast, and accurate algorithm to estimate large phylogenies by maximum likelihood. *Syst. Biol.* 52, 696–704.
- Haghverdi, L., Lun, A.T.L., Morgan, M.D., and Marioni, J.C. (2018). Batch effects in single-cell RNA-sequencing data are corrected by matching mutual nearest neighbors. *Nat. Biotechnol.* 36, 421–427.
- Heinz, S., Benner, C., Spann, N., Bertolino, E., Lin, Y.C., Laslo, P., Cheng, J.X., Murre, C., Singh, H., and Glass, C.K. (2010). Simple combinations of lineage-determining transcription factors prime cis-regulatory elements required for macrophage and B cell identities. *Mol. Cell* 38, 576–589.
- Hocker, J.D., Poirion, O.B., Zhu, F., Buchanan, J., Zhang, K., Chiou, J., Wang, T.-M., Zhang, Q., Hou, X., Li, Y.E., et al. (2021). Cardiac Cell Type-Specific Gene Regulatory Programs and Disease Risk Association. *Sci Adv* 7, eabf1444.
- Hoffmann, T.J., Theusch, E., Haldar, T., Ranatunga, D.K., Jorgenson, E., Medina, M.W., Kvale, M.N., Kwok, P.Y., Schaefer, C., Krauss, R.M., et al. (2018). A large electronic-health-record-based genome-wide study of serum lipids. *Nat. Genet.* 50, 401–413.
- International Multiple Sclerosis Genetics Consortium (2019). Multiple sclerosis genomic map implicates peripheral immune cells and microglia in susceptibility. *Science* 365, eaav7188.
- Jansen, I.E., Savage, J.E., Watanabe, K., Bryois, J., Williams, D.M., Steinberg, S., Sealock, J., Karlsson, I.K., Hägg, S., Athanasiu, L., et al. (2019). Genome-wide meta-analysis identifies new loci and functional pathways influencing Alzheimer's disease risk. *Nat. Genet.* 51, 404–413.
- Jedlicka, P., Sui, X., Sussel, L., and Gutierrez-Hartmann, A. (2009). Ets transcription factors control epithelial maturation and transit and crypt-villus morphogenesis in the mammalian intestine. *Am. J. Pathol.* 174, 1280–1290.
- Ji, S.G., Juran, B.D., Mucha, S., Folseraas, T., Jostins, L., Melum, E., Kumasaka, N., Atkinson, E.J., Schlicht, E.M., Liu, J.Z., et al.; UK-PSC Consortium; International IBD Genetics Consortium; International PSC Study Group (2017). Genome-wide association study of primary sclerosing cholangitis identifies new risk loci and quantifies the genetic relationship with inflammatory bowel disease. *Nat. Genet.* 49, 269–273.
- Jin, Y., Andersen, G., Yorgov, D., Ferrara, T.M., Ben, S., Brownson, K.M., Holland, P.J., Birlea, S.A., Siebert, J., Hartmann, A., et al. (2016). Genome-wide association studies of autoimmune vitiligo identify 23 new risk loci and highlight key pathways and regulatory variants. *Nat. Genet.* 48, 1418–1424.
- John, S., Sabo, P.J., Canfield, T.K., Lee, K., Vong, S., Weaver, M., Wang, H., Vierstra, J., Reynolds, A.P., Thurman, R.E., and Stamatoyannopoulos, J.A. (2013). Genome-Scale Mapping of DNase I Hypersensitivity. *Curr. Protoc. Mol. Biol.* Chapter 27, Unit 21.27.
- Jung, I., Schmitt, A., Diao, Y., Lee, A.J., Liu, T., Yang, D., Tan, C., Eom, J., Chan, M., Chee, S., et al. (2019). A compendium of promoter-centered long-range chromatin interactions in the human genome. *Nat. Genet.* 51, 1442–1449.
- Kemp, J.P., Morris, J.A., Medina-Gomez, C., Forgetta, V., Warrington, N.M., Youlten, S.E., Zheng, J., Gregson, C.L., Grundberg, E., Trajanoska, K., et al. (2017). Identification of 153 new loci associated with heel bone mineral density and functional involvement of GPC6 in osteoporosis. *Nat. Genet.* 49, 1468–1475.
- Kent, W.J., Sugnet, C.W., Furey, T.S., Roskin, K.M., Pringle, T.H., Zahler, A.M., and Haussler, D. (2002). The human genome browser at UCSC. *Genome Res.* 12, 996–1006.
- Kilpeläinen, T.O., Carli, J.F., Skowronski, A.A., Sun, Q., Kriebel, J., Feitosa, M.F., Hedman, Å.K., Drong, A.W., Hayes, J.E., Zhao, J., et al. (2016). Genome-wide meta-analysis uncovers novel loci influencing circulating leptin levels. *Nat. Commun.* 7, 10494.
- Klein, A.M., Mazutis, L., Akartuna, I., Tallapragada, N., Veres, A., Li, V., Peshkin, L., Weitz, D.A., and Kirschner, M.W. (2015). Droplet barcoding for single-cell transcriptomics applied to embryonic stem cells. *Cell* 161, 1187–1201.
- Klemm, S.L., Shipony, Z., and Greenleaf, W.J. (2019). Chromatin accessibility and the regulatory epigenome. *Nat. Rev. Genet.* 20, 207–220.
- Kundaje, A., Meuleman, W., Ernst, J., Bilenky, M., Yen, A., Heravi-Moussavi, A., Kheradpour, P., Zhang, Z., Wang, J., Ziller, M.J., et al.; Roadmap Epigenomics Consortium (2015). Integrative analysis of 111 reference human epigenomes. *Nature* 518, 317–330.
- Lake, B.B., Chen, S., Sos, B.C., Fan, J., Kaeser, G.E., Yung, Y.C., Duong, T.E., Gao, D., Chun, J., Kharchenko, P.V., and Zhang, K. (2018). Integrative single-cell analysis of transcriptional and epigenetic states in the human adult brain. *Nat. Biotechnol.* 36, 70–80.
- Lareau, C.A., Duarte, F.M., Chew, J.G., Kartha, V.K., Burkett, Z.D., Kohlway, A.S., Pokholok, D., Aryee, M.J., Steemers, F.J., Lebofsky, R., and Buenrostro, J.D. (2019). Droplet-based combinatorial indexing for massive-scale single-cell chromatin accessibility. *Nat. Biotechnol.* 37, 916–924.
- Li, H., and Durbin, R. (2009). Fast and accurate short read alignment with Burrows-Wheeler transform. *Bioinformatics* 25, 1754–1760.
- Li, Y.E., Preissl, S., Hou, X., Zhang, Z., Zhang, K., Qiu, Y., Poirion, O.B., Li, B., Chiou, J., Liu, H., et al. (2021). An atlas of gene regulatory elements in adult mouse cerebrum. *Nature* 598, 129–136.
- Litviňuková, M., Talavera-López, C., Maatz, H., Reichart, D., Worth, C.L., Lindberg, E.L., Kanda, M., Polanski, K., Heinig, M., Lee, M., et al. (2020). Cells of the adult human heart. *Nature* 588, 466–472.
- Luo, C., Keown, C.L., Kurihara, L., Zhou, J., He, Y., Li, J., Castanon, R., Lucero, J., Nery, J.R., Sandoval, J.P., et al. (2017a). Single-cell methylomes identify neuronal subtypes and regulatory elements in mammalian cortex. *Science* 357, 600–604.
- Luo, Y., de Lange, K.M., Jostins, L., Moutsianas, L., Randall, J., Kennedy, N.A., Lamb, C.A., McCarthy, S., Ahmad, T., Edwards, C., et al. (2017b). Exploring the genetic architecture of inflammatory bowel disease by whole-genome sequencing identifies association at ADCY7. *Nat. Genet.* 49, 186–192.
- Macosko, E.Z., Basu, A., Satija, R., Nemesh, J., Shekhar, K., Goldman, M., Tirsh, I., Bialas, A.R., Kamitaki, N., Martersteck, E.M., et al. (2015). Highly Parallel Genome-wide Expression Profiling of Individual Cells Using Nanoliter Droplets. *Cell* 161, 1202–1214.
- Mahajan, A., Taliun, D., Thurner, M., Robertson, N.R., Torres, J.M., Rayner, N.W., Payne, A.J., Steinthorsdottir, V., Scott, R.A., Grarup, N., et al. (2018). Fine-mapping type 2 diabetes loci to single-variant resolution using high-density imputation and islet-specific epigenome maps. *Nat. Genet.* 50, 1505–1513.
- Malik, R., Chauhan, G., Traylor, M., Sargurupremraj, M., Okada, Y., Mishra, A., Rutten-Jacobs, L., Giese, A.K., van der Laan, S.W., Gretarsdottir, S., et al.; AF-Gen Consortium; Cohorts for Heart and Aging Research in Genomic Epidemiology (CHARGE) Consortium; International Genomics of Blood Pressure (iGEN-BP) Consortium; INVENT Consortium; STARNET; BioBank Japan Cooperative Hospital Group; COMPASS Consortium; EPIC-CVD Consortium; EPIC-InterAct Consortium; International Stroke Genetics Consortium (ISGC); METASTROKE Consortium; Neurology Working Group of the CHARGE Consortium; NINDS Stroke Genetics Network (SiGN); UK Young Lacunar DNA Study; MEGASTROKE Consortium (2018). Multiancestry genome-wide association study of 520,000 subjects identifies 32 loci associated with stroke and stroke subtypes. *Nat. Genet.* 50, 524–537.

- Manning, A.K., Hivert, M.F., Scott, R.A., Grimsby, J.L., Bouatia-Naji, N., Chen, H., Rybin, D., Liu, C.T., Bielak, L.F., Prokopenko, I., et al.; DIAbetes Genetics Replication And Meta-analysis (DIAGRAM) Consortium; Multiple Tissue Human Expression Resource (MUTHER) Consortium (2012). A genome-wide approach accounting for body mass index identifies genetic variants influencing fasting glycemic traits and insulin resistance. *Nat. Genet.* 44, 659–669.
- Maurano, M.T., Humbert, R., Rynes, E., Thurman, R.E., Haugen, E., Wang, H., Reynolds, A.P., Sandstrom, R., Qu, H., Brody, J., et al. (2012). Systematic localization of common disease-associated variation in regulatory DNA. *Science* 337, 1190–1195.
- McInnes, L., Healy, J., and Melville, J. (2018). Umap: Uniform manifold approximation and projection for dimension reduction. *arXiv*, arXiv:1802.03426.
- McLean, C.Y., Bristor, D., Hiller, M., Clarke, S.L., Schaar, B.T., Lowe, C.B., Wenger, A.M., and Bejerano, G. (2010). GREAT improves functional interpretation of cis-regulatory regions. *Nat. Biotechnol.* 28, 495–501.
- Meuleman, W., Muratov, A., Rynes, E., Halow, J., Lee, K., Bates, D., Diegel, M., Dunn, D., Neri, F., Teodosiadis, A., et al. (2020). Index and biological spectrum of human DNase I hypersensitive sites. *Nature* 584, 244–251.
- Michailidou, K., Lindström, S., Dennis, J., Beesley, J., Hui, S., Kar, S., Lemäçon, A., Soucy, P., Glubb, D., Rostamianfar, A., et al.; NBCS Collaborators; ABCTB Investigators; ConFab/AOCS Investigators (2017). Association analysis identifies 65 new breast cancer risk loci. *Nature* 551, 92–94.
- Moore, J.E., Purcaro, M.J., Pratt, H.E., Epstein, C.B., Shores, N., Adrian, J., Kawli, T., Davis, C.A., Dobin, A., Kaul, R., et al.; ENCODE Project Consortium (2020). Expanded encyclopaedias of DNA elements in the human and mouse genomes. *Nature* 583, 699–710.
- Nasser, J., Bergman, D.T., Fulco, C.P., Guckelberger, P., Doughty, B.R., Patwardhan, T.A., Jones, T.R., Nguyen, T.H., Ulirsch, J.C., Natri, H.M., et al. (2021). Genome-wide enhancer maps link risk variants to disease genes. *Nature* 593, 238–243.
- Nielsen, J.B., Thorolfsdottir, R.B., Fritzsche, L.G., Zhou, W., Skov, M.W., Graham, S.E., Herron, T.J., McCarthy, S., Schmidt, E.M., Sveinbjörnsson, G., et al. (2018). Biobank-driven genomic discovery yields new insight into atrial fibrillation biology. *Nat. Genet.* 50, 1234–1239.
- Nikpay, M., Goel, A., Won, H.H., Hall, L.M., Willenborg, C., Kanoni, S., Saleheen, D., Kyriakou, T., Nelson, C.P., Hopewell, J.C., et al. (2015). A comprehensive 1,000 Genomes-based genome-wide association meta-analysis of coronary artery disease. *Nat. Genet.* 47, 1121–1130.
- Okada, Y., Wu, D., Trynka, G., Raj, T., Terao, C., Ikari, K., Kochi, Y., Ohmura, K., Suzuki, A., Yoshida, S., et al.; RACI consortium; GARNET consortium (2014). Genetics of rheumatoid arthritis contributes to biology and drug discovery. *Nature* 506, 376–381.
- Paterno, L., Standl, M., Waage, J., Baurecht, H., Hotze, M., Strachan, D.P., Curtin, J.A., Bønnelykke, K., Tian, C., Takahashi, A., et al.; Australian Asthma Genetics Consortium (AAGC) (2015). Multi-ancestry genome-wide association study of 21,000 cases and 95,000 controls identifies new risk loci for atopic dermatitis. *Nat. Genet.* 47, 1449–1456.
- Perrino, C., and Rockman, H.A. (2006). GATA4 and the two sides of gene expression reprogramming. *Circ. Res.* 98, 715–716.
- Pividori, M., Schoettler, N., Nicolae, D.L., Ober, C., and Im, H.K. (2019). Shared and distinct genetic risk factors for childhood-onset and adult-onset asthma: genome-wide and transcriptome-wide studies. *Lancet Respir. Med.* 7, 509–522.
- Pliner, H.A., Packer, J.S., McFaline-Figueroa, J.L., Cusanovich, D.A., Daza, R.M., Aghamirzaie, D., Srivatsan, S., Qiu, X., Jackson, D., Minkina, A., et al. (2018). Cicero Predicts cis-Regulatory DNA Interactions from Single-Cell Chromatin Accessibility Data. *Mol. Cell* 71, 858–871.e8.
- Pollard, K.S., Hubisz, M.J., Rosenbloom, K.R., and Siepel, A. (2010). Detection of nonneutral substitution rates on mammalian phylogenies. *Genome Res.* 20, 110–121.
- Pownall, M.E., Gustafsson, M.K., and Emerson, C.P., Jr. (2002). Myogenic regulatory factors and the specification of muscle progenitors in vertebrate embryos. *Annu. Rev. Cell Dev. Biol.* 18, 747–783.
- Preissl, S., Fang, R., Huang, H., Zhao, Y., Raviram, R., Gorkin, D.U., Zhang, Y., Sos, B.C., Afzal, V., Dickel, D.E., et al. (2018). Single-nucleus analysis of accessible chromatin in developing mouse forebrain reveals cell-type-specific transcriptional regulation. *Nat. Neurosci.* 21, 432–439.
- Sakornsakopat, P., Prokopenko, D., Lamontagne, M., Reeve, N.F., Guyatt, A.L., Jackson, V.E., Shrine, N., Qiao, D., Bartz, T.M., Kim, D.K., et al.; Spiro-Meta Consortium; International COPD Genetics Consortium (2019). Genetic landscape of chronic obstructive pulmonary disease identifies heterogeneous cell-type and phenotype associations. *Nat. Genet.* 51, 494–505.
- Salem, S., Salem, D., and Gros, P. (2020). Role of IRF8 in immune cells functions, protection against infections, and susceptibility to inflammatory diseases. *Hum. Genet.* 139, 707–721.
- Saxena, R., Hivert, M.F., Langenberg, C., Tanaka, T., Pankow, J.S., Vollenweider, P., Lyssenko, V., Bouatia-Naji, N., Dupuis, J., Jackson, A.U., et al.; GIANT consortium; MAGIC investigators (2010). Genetic variation in GIPR influences the glucose and insulin responses to an oral glucose challenge. *Nat. Genet.* 42, 142–148.
- Schafmayer, C., Harrison, J.W., Buch, S., Lange, C., Reichert, M.C., Hofer, P., Cossais, F., Kucinskas, J., von Schönfels, W., Schniewind, B., et al. (2019). Genome-wide association analysis of diverticular disease points towards neuromuscular, connective tissue and epithelial pathomechanisms. *Gut* 68, 854–865.
- Schaid, D.J., Chen, W., and Larson, N.B. (2018). From genome-wide associations to candidate causal variants by statistical fine-mapping. *Nat. Rev. Genet.* 19, 491–504.
- Schiaffino, S., and Reggiani, C. (2011). Fiber types in mammalian skeletal muscles. *Physiol. Rev.* 91, 1447–1531.
- Schiaffino, S., Rossi, A.C., Smerdu, V., Leinwand, L.A., and Reggiani, C. (2015). Developmental myosins: expression patterns and functional significance. *Skelet. Muscle* 5, 22.
- Schug, J., Schuller, W.P., Kappen, C., Salbaum, J.M., Bucan, M., and Stoeckert, C.J., Jr. (2005). Promoter features related to tissue specificity as measured by Shannon entropy. *Genome Biol.* 6, R33.
- Shadrina, A.S., Sharapov, S.Z., Shashkova, T.I., and Tsepilov, Y.A. (2019). Varicose veins of lower extremities: Insights from the first large-scale genetic study. *PLoS Genet.* 15, e1008110.
- Shen, T., Aneas, I., Sakabe, N., Dirschniger, R.J., Wang, G., Smemo, S., Westlund, J.M., Cheng, H., Dalton, N., Gu, Y., et al. (2011). Tbx20 regulates a genetic program essential to adult mouse cardiomyocyte function. *J. Clin. Invest.* 121, 4640–4654.
- Shen, Y., Yue, F., McCleary, D.F., Ye, Z., Edsall, L., Kuan, S., Wagner, U., Dixon, J., Lee, L., Lobanenkov, V.V., and Ren, B. (2012). A map of the cis-regulatory sequences in the mouse genome. *Nature* 488, 116–120.
- Shlyueva, D., Stampfel, G., and Stark, A. (2014). Transcriptional enhancers: from properties to genome-wide predictions. *Nat. Rev. Genet.* 15, 272–286.
- Shrine, N., Guyatt, A.L., Erzurumluoglu, A.M., Jackson, V.E., Hobbs, B.D., Melbourne, C.A., Batini, C., Fawcett, K.A., Song, K., Sakornsakopat, P., et al.; Understanding Society Scientific Group (2019). New genetic signals for lung function highlight pathways and chronic obstructive pulmonary disease associations across multiple ancestries. *Nat. Genet.* 51, 481–493.
- Singh, M.K., Christoffels, V.M., Dias, J.M., Trowe, M.-O., Petry, M., Schuster-Gossler, K., Bürger, A., Ericson, J., and Kispert, A. (2005). Tbx20 is essential for cardiac chamber differentiation and repression of Tbx2. *Development* 132, 2697–2707.
- Sinnamon, J.R., Torkenczy, K.A., Linhoff, M.W., Vitak, S.A., Mulqueen, R.M., Pliner, H.A., Trapnell, C., Steemers, F.J., Mandel, G., and Adey, A.C. (2019). The accessible chromatin landscape of the murine hippocampus at single-cell resolution. *Genome Res.* 29, 857–869.
- Stranger, B.E., Brigham, L.E., Hasz, R., Hunter, M., Johns, C., Johnson, M., Kopen, G., Leinweber, W.F., Lonsdale, J.T., McDonald, A., et al.; eGTEX Project (2017). Enhancing GTEx by bridging the gaps between genotype, gene expression, and disease. *Nat. Genet.* 49, 1664–1670.

- Strawbridge, R.J., Dupuis, J., Prokopenko, I., Barker, A., Ahlqvist, E., Rybin, D., Petrie, J.R., Travers, M.E., Bouatia-Naji, N., Dimas, A.S., et al.; DIAGRAM Consortium; GIANT Consortium; MuTHER Consortium; CARDIoGRAM Consortium; C4D Consortium (2011). Genome-wide association identifies nine common variants associated with fasting proinsulin levels and provides new insights into the pathophysiology of type 2 diabetes. *Diabetes* 60, 2624–2634.
- Stuart, C.A., Stone, W.L., Howell, M.E., Brannon, M.F., Hall, H.K., Gibson, A.L., and Stone, M.H. (2016). Myosin content of individual human muscle fibers isolated by laser capture microdissection. *Am. J. Physiol. Cell Physiol.* 310, C381–C389.
- Tachmazidou, I., Hatzikotoulas, K., Southam, L., Esparza-Gordillo, J., Haberland, V., Zheng, J., Johnson, T., Koprulu, M., Zengini, E., Steinberg, J., et al.; arcOGEN Consortium (2019). Identification of new therapeutic targets for osteoarthritis through genome-wide analyses of UK Biobank data. *Nat. Genet.* 51, 230–236.
- Teumer, A., Chaker, L., Groeneweg, S., Li, Y., Di Munno, C., Barbieri, C., Schultheiss, U.T., Traglia, M., Ahluwalia, T.S., Akiyama, M., et al.; Lifelines Cohort Study (2018). Genome-wide analyses identify a role for SLC17A4 and AADAT in thyroid hormone regulation. *Nat. Commun.* 9, 4455.
- Tin, A., Marten, J., Halperin Kuhns, V.L., Li, Y., Wuttke, M., Kirsten, H., Sieber, K.B., Qiu, C., Gorski, M., Yu, Z., et al.; German Chronic Kidney Disease Study; Lifelines Cohort Study; V. A. Million Veteran Program (2019). Target genes, variants, tissues and transcriptional pathways influencing human serum urate levels. *Nat. Genet.* 51, 1459–1474.
- Traag, V.A., Van Dooren, P., and Nesterov, Y. (2011). Narrow scope for resolution-limit-free community detection. *Phys. Rev. E Stat. Nonlin. Soft Matter Phys.* 84, 016114.
- Traag, V.A., Waltman, L., and van Eck, N.J. (2019). From Louvain to Leiden: guaranteeing well-connected communities. *Sci. Rep.* 9, 5233.
- Trevino, A.E., Müller, F., Andersen, J., Sundaram, L., Kathiria, A., Shcherbina, A., Farh, K., Chang, H.Y., Paşa, A.M., Kundaje, A., et al. (2021). Chromatin and gene-regulatory dynamics of the developing human cerebral cortex at single-cell resolution. *Cell* 184, 5053–5069.e23.
- Vierstra, J., Lazar, J., Sandstrom, R., Halow, J., Lee, K., Bates, D., Diegel, M., Dunn, D., Neri, F., Haugen, E., et al. (2020). Global reference mapping of human transcription factor footprints. *Nature* 583, 729–736.
- Visel, A., Minovitsky, S., Dubchak, I., and Pennacchio, L.A. (2007). VISTA Enhancer Browser—a database of tissue-specific human enhancers. *Nucleic Acids Res.* 35, D88–D92.
- Wakefield, J. (2009). Bayes factors for genome-wide association studies: comparison with P-values. *Genet. Epidemiol.* 33, 79–86.
- Wang, A., Chiou, J., Poirion, O.B., Buchanan, J., Valdez, M.J., Verheyden, J.M., Hou, X., Kudtarkar, P., Narendra, S., Newsome, J.M., et al.; NHLBI Lung-Map Consortium (2020). Single-cell multiomic profiling of human lungs reveals cell-type-specific and age-dynamic control of SARS-CoV2 host genes. *eLife* 9, e62522.
- Warrington, N.M., Beaumont, R.N., Horikoshi, M., Day, F.R., Helgeland, Ø., Laurin, C., Bacelis, J., Peng, S., Hao, K., Feenstra, B., et al.; EGG Consortium (2019). Maternal and fetal genetic effects on birth weight and their relevance to cardio-metabolic risk factors. *Nat. Genet.* 51, 804–814.
- Watanabe, K., Stringer, S., Frei, O., Umićević Mirkov, M., de Leeuw, C., Polderman, T.J.C., van der Sluis, S., Andreassen, O.A., Neale, B.M., and Posthuma, D. (2019). A global overview of pleiotropy and genetic architecture in complex traits. *Nat. Genet.* 51, 1339–1348.
- Wiberg, A., Ng, M., Schmid, A.B., Smillie, R.W., Baskozos, G., Holmes, M.V., Künnapuu, K., Mägi, R., Bennett, D.L., and Furniss, D. (2019). A genome-wide association analysis identifies 16 novel susceptibility loci for carpal tunnel syndrome. *Nat. Commun.* 10, 1030.
- Wolock, S.L., Lopez, R., and Klein, A.M. (2019). Scrublet: Computational Identification of Cell Doublets in Single-Cell Transcriptomic Data. *Cell Syst.* 8, 281–291.e9.
- Wuttke, M., Li, Y., Li, M., Sieber, K.B., Feitosa, M.F., Gorski, M., Tin, A., Wang, L., Chu, A.Y., Hoppmann, A., et al.; Lifelines Cohort Study; V. A. Million Veteran Program (2019). A catalog of genetic loci associated with kidney function from analyses of a million individuals. *Nat. Genet.* 51, 957–972.
- Yan, M., Wang, H., Sun, J., Liao, W., Li, P., Zhu, Y., Xu, C., Joo, J., Sun, Y., Abbasi, S., et al. (2016). Cutting Edge: Expression of IRF8 in Gastric Epithelial Cells Confers Protective Innate Immunity against Helicobacter pylori Infection. *J. Immunol.* 196, 1999–2003.
- Yan, J., Qiu, Y., dos Santos, A.M.R., Yin, Y., Li, Y.E., Vinckier, N., Nariai, N., Benaglio, P., Raman, A., Li, X., et al. (2021). Systematic Analysis of Transcription Factor Binding to Noncoding Variants in the Human Genome. *Nature* 591, 147–151.
- Yang, J., Benyamin, B., McEvoy, B.P., Gordon, S., Henders, A.K., Nyholt, D.R., Madden, P.A., Heath, A.C., Martin, N.G., Montgomery, G.W., et al. (2010). Common SNPs explain a large proportion of the heritability for human height. *Nat. Genet.* 42, 565–569.
- Zhang, Y., Liu, T., Meyer, C.A., Eeckhoute, J., Johnson, D.S., Bernstein, B.E., Nusbaum, C., Myers, R.M., Brown, M., Li, W., and Liu, X.S. (2008). Model-based analysis of ChIP-Seq (MACS). *Genome Biol.* 9, R137.
- Zhang, K., Wang, M., Zhao, Y., and Wang, W. (2019). Taiji: System-level identification of key transcription factors reveals transcriptional waves in mouse embryonic development. *Sci. Adv.* 5, eaav3262.
- Zhu, C., Preissl, S., and Ren, B. (2020). Single-cell multimodal omics: the power of many. *Nat. Methods* 17, 11–14.

## STAR★METHODS

### KEY RESOURCES TABLE

REAGENT or RESOURCE	SOURCE	IDENTIFIER
<b>Biological samples</b>		
Adult Human Tissue Samples	ENTEx Collaboration	<a href="https://www.encodeproject.org/entex-matrix/?type=Experiment&amp;status=released&amp;internal_tags=ENTEx">https://www.encodeproject.org/entex-matrix/?type=Experiment&amp;status=released&amp;internal_tags=ENTEx</a>
<b>Chemicals, peptides, and recombinant proteins</b>		
Tn5 transposase	QB3 Macrolab at UC Berkeley	N/A
SPRISelect reagent	Beckman Coulter	Cat# B23319
DRAQ7	Cell Signaling	Cat# 7406
NEBNext High-Fidelity PCR Master Mix	NEB	Cat# M0541L
LightCycler 480 SYBR Green I Master Mix	Roche	Cat# 04707516001
<b>Critical commercial assays</b>		
gentleMACS Octo Dissociator	Miltenyi	Cat# 130-095-937
<b>Deposited data</b>		
sci-ATAC-seq data of human adult tissues	This paper	GEO: GSE184462
sci-ATAC-seq data of human lung samples	<a href="#">Wang et al., 2020</a>	dbGaP: phs001961
sci-ATAC-seq data of human heart samples	<a href="#">(Hocker et al., 2021)</a>	dbGaP: phs002204
sci-ATAC-seq data of human islet samples	<a href="#">(Chiou et al., 2021)</a>	GEO: GSE160472
sci-ATAC-seq data of human fetal tissues	<a href="#">Domcke et al., 2020</a>	<a href="https://descartes.brotmanbaty.org/bbi/human-chromatin-during-development/">https://descartes.brotmanbaty.org/bbi/human-chromatin-during-development/</a> dbGaP: phs002003
raw data used to produce the figures	This paper	Mendeley Data: 10.17632/yv4fzv6cnm.1
<b>Oligonucleotides</b>		
Custom Tagmentation Oligos	This paper	<a href="#">Table S6</a>
Custom PCR Primers	This paper	<a href="#">Table S6</a>
Custom Sequencing Primers	This paper	<a href="#">Table S6</a>
<b>Software and algorithms</b>		
BWA version 0.7.17	<a href="#">Li and Durbin, 2009</a>	<a href="https://github.com/lh3/bwa">https://github.com/lh3/bwa</a>
Samtools version 1.9	<a href="#">Danecek et al., 2021</a>	<a href="https://github.com/samtools/samtools">https://github.com/samtools/samtools</a>
Taiji version 1.3.0	<a href="#">Zhang et al., 2019</a>	<a href="https://github.com/Taiji-pipeline/Taiji">https://github.com/Taiji-pipeline/Taiji</a>
Python package: taiji-utils version 0.2.3	This paper	<a href="https://pypi.org/project/taiji-utils/">https://pypi.org/project/taiji-utils/</a>
liftOver	<a href="#">Kent et al., 2002</a>	<a href="http://hgdownload.soe.ucsc.edu/admin/exe/linux.x86_64/liftOver">http://hgdownload.soe.ucsc.edu/admin/exe/linux.x86_64/liftOver</a>
ATACdemultiplex version 0.46.12	This paper	<a href="https://gitlab.com/Groumf/ATACdemultiplex/">https://gitlab.com/Groumf/ATACdemultiplex/</a>
bedGraphToBigWig	<a href="#">Kent et al., 2002</a>	<a href="http://hgdownload.soe.ucsc.edu/admin/exe/linux.x86_64/bedGraphToBigWig">http://hgdownload.soe.ucsc.edu/admin/exe/linux.x86_64/bedGraphToBigWig</a>
R version 4.0.5	R Foundation for Statistical Computing	<a href="https://www.r-project.org/">https://www.r-project.org/</a>
Python version 3.8	Python Software Foundation	<a href="https://www.python.org/">https://www.python.org/</a>
Python package: umap-learn version 0.5.0	<a href="#">(McInnes et al., 2018)</a>	<a href="https://pypi.org/project/umap-learn/">https://pypi.org/project/umap-learn/</a>
Python package: scrublet	<a href="#">Wolock et al., 2019</a>	<a href="https://github.com/swolock/scrublet">https://github.com/swolock/scrublet</a>
GREAT version 4.0.4	<a href="#">McLean et al., 2010</a>	<a href="http://great.stanford.edu/public/html/">http://great.stanford.edu/public/html/</a>

## RESOURCE AVAILABILITY

### Lead contact

Further information and request for resources and reagents should be directed to and will be fulfilled by the lead contact, Bing Ren ([biren@health.ucsd.edu](mailto:biren@health.ucsd.edu)).

### Materials availability

This study did not generate new unique reagents.

### Data and code availability

- Single-nucleus ATAC-seq datasets generated in this study have been deposited at GEO and are publicly available as of the date of publication. Accession numbers are listed in the [Key Resources Table](#) and [Table S2](#). This paper analyzes existing, publicly available data. These accession numbers for these datasets are listed in the [Key Resources Table](#). Raw data from [Figures 1, 2, 4, 6, S4](#) and [S6](#) were deposited on Mendeley at 10.17632/yv4fv6cnm.1.
- All original code has been deposited at Github and is publicly available as of the date of publication. Links are listed in the [Key Resources Table](#).
- Any additional information required to reanalyze the data reported in this paper is available from the lead contact upon request.

## EXPERIMENTAL MODEL AND SUBJECT DETAILS

### Human Subjects

Adult human tissue samples were acquired by the ENTEx collaborative project ([Stranger et al., 2017](#)) via the GTEx collection pipeline ([Carithers et al., 2015](#)). Donor characteristics including age and sex are provided in [Table S1](#). All human donors were deceased, and informed consent was obtained via next-of-kin consent for the collection and banking of deidentified tissue samples for scientific research. Donor eligibility requirements were as described previously ([Carithers et al., 2015](#)), and excluded individuals with metastatic cancer and individuals who had received chemotherapy for cancer within the prior two years.

## METHOD DETAILS

### Tissue feasibility testing for sci-ATAC-seq

Frozen tissue samples were sectioned on dry ice into two aliquots of equivalent mass. For nuclear isolation, one aliquot was subjected to manual pulverization via mortar and pestle while submerged in liquid nitrogen, and the other aliquot was homogenized in a gentleMACS M-tube (Miltenyi) on a gentleMACS Octo Dissociator (Miltenyi) using the “Protein\_01\_01” protocol in MACS buffer (5 mM CaCl<sub>2</sub>, 2 mM EDTA, 1X protease inhibitor (Roche, 05-892-970-001), 3 mM MgAc, 10 mM Tris-HCL pH 8, 0.6 mM DTT) and pelleted with a swinging bucket centrifuge (500 x g, 5 min, 4°C; 5920R, Eppendorf). Pulverized frozen tissue and pelleted nuclei from gentleMACS M-tubes were each split into two further aliquots. One aliquot from each of the two nuclear isolation conditions was then resuspended in 1 mL Nuclear Permeabilization Buffer (1X PBS, 5% Bovine Serum Albumin, 0.2% IGEPAL CA-630 (Sigma), 1 mM DTT, 1X Protease inhibitor), and the other aliquot from the same nuclear isolation condition was resuspended in 1 mL OMNI Buffer (10mM Tris-HCL (pH 7.5), 10mM NaCl, 3mM MgCl<sub>2</sub>, 0.1% Tween-20 (Sigma), 0.1% IGEPAL-CA630 (Sigma) and 0.01% Digitonin (Promega) in water), yielding a total of four nuclear isolation/nuclear permeabilization buffer conditions tested for each tissue type. Nuclei were rotated at 4°C for 5 minutes before being pelleted again with a swinging bucket centrifuge (500 x g, 5 min, 4°C; 5920R, Eppendorf). After centrifugation, permeabilized nuclei were resuspended in 500 µL high salt fragmentation buffer (36.3 mM Tris-acetate (pH = 7.8), 72.6 mM potassium-acetate, 11 mM Mg-acetate, 17.6% DMF) and counted using a hemocytometer. Concentration was adjusted to 2,000 nuclei/9 µL, and 2,000 nuclei were dispensed 12 wells of a 96-well plate per nuclear isolation/permeabilization condition (samples were processed in batches of 4 nuclear isolation/permeabilization conditions per 2 different tissue samples). For fragmentation, 1 µL barcoded Tn5 transposomes ([Table S6](#)) were added using a BenchSmart 96 (Mettler Toledo), mixed five times, and incubated for 60 min at 37°C with shaking (500 rpm). To inhibit the Tn5 reaction, 10 µL of 40 mM EDTA (final 20mM) were added to each well with a BenchSmart 96 (Mettler Toledo) and the plate was incubated at 37°C for 15 min with shaking (500 rpm). Next, 20 µL of 2x sort buffer (2% BSA, 2 mM EDTA in PBS) were added using a BenchSmart 96 (Mettler Toledo). All 12 wells from each nuclear isolation/permeabilization condition were combined into a separate FACS tube, and stained with Draq7 at 1:150 dilution (Cell Signaling). For each nuclear isolation/permeabilization condition, we used a SH800 (Sony) to sort four wells containing 0 nuclei per well and four wells containing 80 nuclei per well into one 96-well plate (total of 768 wells) containing 10.5 µL EB (25 pmol primer i7, 25 pmol primer i5, 200 ng BSA (Sigma)). After addition of 1 µL 0.2% SDS using a BenchSmart 96 (Mettler Toledo), the 96 well plate was incubated at 55°C for 7 min with shaking (500 rpm). 1 µL 12.5% Triton-X was added to each well to quench the SDS. Next, 12.5 µL NEBNext High-Fidelity 2 × PCR Master Mix (NEB) were added to each well and samples were PCR-amplified (72°C 5 min, 98°C 30 s, (98°C 10 s, 63°C 30 s, 72°C 60 s) × 12 cycles, held at 12°C). After PCR, all wells were assayed for DNA library concentration using the PerfeCTa NGS Quantification RT-qPCR Kit (Quanta Biosciecnces) according to manufacturer's

protocols, and subsequently returned to the thermal cycler for a second round of PCR amplification ( $72^{\circ}\text{C}$  5 min,  $98^{\circ}\text{C}$  30 s, ( $98^{\circ}\text{C}$  10 s,  $63^{\circ}\text{C}$  30 s,  $72^{\circ}\text{C}$  60 s)  $\times$  4 cycles, held at  $12^{\circ}\text{C}$ ). After the second PCR amplification, for each nuclear isolation/permeabilization condition, wells containing 0 nuclei were combined and wells containing 80 nuclei were combined. The resulting DNA libraries were purified according to the MinElute PCR Purification Kit manual (QIAGEN) and size selection was performed with SPRISelect reagent (Beckmann Coulter, 0.55x and 1.5x). Final libraries were quantified using a Qubit fluorimeter (Life technologies) and a nucleosomal pattern of fragment size distribution was verified using a Tapestation (High Sensitivity D1000, Agilent). We calculated a signal to noise ratio for final feasibility test libraries using LightCycler® 480 SYBR Green I Master Mix (Roche) along with custom primers for the promoter of human GAPDH (5'-CATCTCAGTCGTTCCAAAGT-3', 5'-TTCCCAGGACTGGACTGT-3') and a heterochromatic gene desert region (5'-CCCAAACCTCTGA GAGGCTTATT-3', 5'-GAGCCATCATCTAGACACCTTC-3'). For each tissue type, the nuclear isolation/permeabilization condition that resulted in optimized nuclear yield (nuclei/mg tissue), library concentrations  $> 50$  pM per 80 sorted nuclei, nucleosomal distribution pattern of fragments, and a  $\log_2(\text{signal to noise ratio}) > 3.3$  was selected for combinatorial indexing-assisted single nucleus ATAC-seq (Table S1).

#### Combinatorial indexing-assisted single nucleus ATAC-seq

Combinatorial indexing-assisted single nucleus ATAC-seq was performed as described previously (Preissl et al., 2018) with slight modifications (Hocker et al., 2021) and using new sets of oligos for tagmentation and PCR (Table S6). Nuclei were isolated and permeabilized according to the optimized conditions from feasibility testing (Table S1). After resuspension in permeabilization buffer, nuclei were rotated at  $4^{\circ}\text{C}$  for 5 minutes before being pelleted again with a swinging bucket centrifuge (500  $\times$  g, 5 min,  $4^{\circ}\text{C}$ ; 5920R, Eppendorf). After centrifugation, permeabilized nuclei were resuspended in 500  $\mu\text{L}$  high salt tagmentation buffer (36.3 mM Tris-acetate ( $\text{pH} = 7.8$ ), 72.6 mM potassium-acetate, 11 mM Mg-acetate, 17.6% DMF) and counted using a hemocytometer. Concentration was adjusted to 2,000 nuclei/ $9 \mu\text{l}$ , and 2,000 nuclei were dispensed into each well of a 96-well plate per sample (96 tagmentation wells/sample, samples were processed in batches of 2-4 samples). For tagmentation, 1  $\mu\text{L}$  barcoded Tn5 transposomes (Table S6) were added using a BenchSmart 96 (Mettler Toledo), mixed five times, and incubated for 60 min at  $37^{\circ}\text{C}$  with shaking (500 rpm). To inhibit the Tn5 reaction, 10  $\mu\text{L}$  of 40 mM EDTA (final 20 mM) were added to each well with a BenchSmart 96 (Mettler Toledo) and the plate was incubated at  $37^{\circ}\text{C}$  for 15 min with shaking (500 rpm). Next, 20  $\mu\text{L}$  of 2x sort buffer (2% BSA, 2 mM EDTA in PBS) were added using a BenchSmart 96 (Mettler Toledo). All wells were combined into a separate FACS tube for each sample, and stained with Draq7 at 1:150 dilution (Cell Signaling). Using a SH800 (Sony), 20 nuclei per sample were sorted per well into eight 96-well plates (total of 768 wells) containing 10.5  $\mu\text{L}$  EB (25 pmol primer i7, 25 pmol primer i5, 200 ng BSA (Sigma)). Preparation of sort plates and all downstream pipetting steps were performed on a Biomek i7 Automated Workstation (Beckman Coulter). After addition of 1  $\mu\text{L}$  0.2% SDS, samples were incubated at  $55^{\circ}\text{C}$  for 7 min with shaking (500 rpm). 1  $\mu\text{L}$  12.5% Triton-X was added to each well to quench the SDS. Next, 12.5  $\mu\text{L}$  NEBNext High-Fidelity 2  $\times$  PCR Master Mix (NEB) were added and samples were PCR-amplified ( $72^{\circ}\text{C}$  5 min,  $98^{\circ}\text{C}$  30 s, ( $98^{\circ}\text{C}$  10 s,  $63^{\circ}\text{C}$  30 s,  $72^{\circ}\text{C}$  60 s)  $\times$  12 cycles, held at  $12^{\circ}\text{C}$ ). After PCR, all wells were combined. Libraries were purified according to the MinElute PCR Purification Kit manual (QIAGEN) using a vacuum manifold (QIAvac 24 plus, QIAGEN) and size selection was performed with SPRISelect reagent (Beckmann Coulter, 0.55x and 1.5x). Libraries were purified one more time with SPRISelect reagent (Beckman Coulter, 1.5x). Libraries were quantified using a Qubit fluorimeter (Life technologies) and a nucleosomal pattern of fragment size distribution was verified using a Tapestation (High Sensitivity D1000, Agilent). Libraries were sequenced on a NextSeq500 or HiSeq4000 sequencer (Illumina) using custom sequencing primers with following read lengths: 50 + 10 + 12 + 50 (Read1 + Index1 + Index2 + Read2). Primer and index sequences are listed in Table S6.

#### Demultiplexing of single nucleus ATAC-seq sequencing reads

For each sequenced single nucleus ATAC-Seq library, we obtained four FASTQ files, two for paired end DNA reads and two for the combinatorial indexes for i5 and T7 (768 and 364 indices, respectively). We selected all reads with up to 2 mismatches per i5 and T7 index (Hamming distance between each pair of indices is 4) and integrated the concatenated barcode at the beginning of the read name in the demultiplexed FASTQ files. The customized scripts can be found at: <https://gitlab.com/Grouumf/ATACdemultiplex/>.

#### Quality control metrics: TSS enrichment and unique fragments

TSS positions were obtained from the GENCODE database v31 (Frankish et al., 2019). Tn5 corrected insertions were aggregated  $\pm$  2000 bp relative (TSS strand-corrected) to each unique TSS genome wide. Then this profile was normalized to the mean accessibility  $\pm$  (1900 to 2000) bp from the TSS and smoothed every 11 bp. The max of the smoothed profile was taken as the TSS enrichment. We then filtered out all single-cells that had fewer than 1,000 unique fragments and/or a TSS enrichment of less than 7 for all datasets.

#### Overall clustering strategy

We utilized multiple rounds of clustering analysis to identify cell clusters. The first round of clustering analysis was performed on individual samples. We divided the genome into 5kb consecutive windows and then scored each cell for any insertions in these windows, generating a window by cell binary matrix for each sample. We filtered out those windows that are generally accessible in all cells for each sample using z-score threshold 1.65. Based on the filtered matrix, we then carried out dimension reduction followed by graph-based clustering to identify cell clusters. We called peaks for each cluster using the aggregated profile of accessibility and then merged the peaks from all clusters to generate a union peak list. Based on the peak list, we generated a cell-by-peak count matrix and

used Scrublet (Wolock et al., 2019) to remove potential doublets. Next, to carry out the second round of clustering analysis, we merged peaks called from all samples to form a reference peak list. We then generated a single binary cell-by-peak matrix using cells from all samples and again performed the dimension reduction followed by graph-based clustering to obtain the major cell groups across the entire dataset. To further dissect cell-type heterogeneity within the major cell groups, we then performed another round of clustering analysis for each of the identified major cell group to identify subclusters.

### Doublet removal

We applied Scrublet to the cell-by-peak count matrix with default parameters. Doublet scores returned by Scrublet were then used to fit a two-component Gaussian mixture model using the “BayesianGaussianMixture” function from the python package “scikit-learn.” The component with larger mean doublet score is presumably formed by doublets and cells belonging to it were removed from downstream analysis.

### Dimension reduction

To find the low-dimensional manifold of the single-cell data, we adapted our previously published method, SnapATAC (Fang et al., 2021), to reduce the dimensionality of the peak by cell count matrix. The previous iteration of SnapATAC utilized spectral embedding for dimension reduction. To increase scalability of spectral embedding, we applied the Nyström method (Bouneffouf and Birol, 2016) for handling large datasets. Specifically, we first randomly sampled 35,000 cells as the training data. We then computed the Jaccard index between each pair of cells in the training set and constructed the similarity matrix  $S$ . We computed the matrix  $P = D^{-1}S$ , where  $D$  is the diagonal matrix such that  $D_{ii} = \sum S_{ij}$ . The eigendecomposition was performed on  $P$  and the eigenvector with eigenvalue 1 was discarded. From the rest of the eigenvectors, we took the first 30 of them corresponding to the largest eigenvalues as the spectral embedding of the training data. We utilized the Nyström method to extend the embedding to the data outside the training set. Given a set of unseen samples, we computed the similarity matrix  $S'$  between the new samples and the training set. The embedding of the new samples is given by  $U' = S'U\Lambda^{-1}$ , where  $U$  and  $\Lambda$  are the eigenvectors and eigenvalues of  $P$  obtained in the previous step.

### Correction of Batch Effects

We performed batch correction for each tissue separately. Inspired by the mutual nearest neighbor batch-effect-correction method (Haghverdi et al., 2018), we developed a variant using mutual nearest centroids to iteratively correct for batch effects in multiple donor samples. Specifically, after dimension reduction we performed k-means clustering on individual replicate or donor sample with k equal to 20. We choose this number because the number of major clusters in a given tissue sample is typically less than 20. We then computed the centroid for each cluster and identified pairs of mutual nearest centroids across different batches. These mutual nearest centroids were used as the anchors to match the cells between different batches and correct for batch effects as described previously (Haghverdi et al., 2018). We found that the result can be further improved by performing above steps iteratively. However, too many iterations may lead to over-correction. We therefore used two iterations in this study.

### Graph-based clustering algorithm

We constructed the k-nearest neighbor graph (k-NNG) using low-dimensional embedding of the cells with k equal to 50. We then applied the Leiden algorithm (Traag et al., 2019) to find communities in the k-NNG corresponding to cell clusters. The Leiden algorithm can be configured to use different quality functions. The modularity model is a popular choice but it suffers from the issue of resolution-limit, particularly when the network is large (Traag et al., 2011). Therefore, we used the modularity model only in the first round of clustering analysis to identify initial clusters. In the final round of clustering, we chose the constant Potts model as the quality function since it is resolution-limit-free and is better suited for identifying rare populations in a large dataset (Traag et al., 2011). To determine the optimal number of clusters, we varied the resolution parameter in the Leiden algorithm and computed the clustering stability and average silhouette score under each resolution. Cluster stability was defined as the consistency, measured by the average adjusted rand index, of results from five independent clustering analyses on perturbed inputs. The perturbation was introduced in a way that 2% of the edges were randomly selected and subjected to removal. We selected the resolution that leads to both high average silhouette score and high clustering stability as well as biological considerations, e.g., number of known cell types in the tissue, marker gene accessibility.

### Peak calling and peak filtering

For each cell cluster, initial peak calling was performed on Tn5-corrected single-base insertions (each end of the Tn5-corrected fragments) using the MACS2 (Zhang et al., 2008) callpeak command with parameters “–shift –100 –extsize 200 –nomodel –call-summits –nolambda –keep-dup all,” filtered by the ENCODE hg38 blacklist (accession: ENCF356LFX). Due to the varying abundance of cell types in each tissue, single-cell assays typically profile different cell types at different sequencing depths. To account for these differences, we adapted peak calling cutoffs to different sequencing depths. Specifically, we choose a cutoff of FDR less than 0.1, 0.05, 0.025, 0.01, and 0.001, corresponding to the situations when the number of reads is within the range of 0-5 million, 5-25 million, 25-50 million, 50-100 million, and 100 million and above. Using simulated datasets, we found that this procedure achieved good balance between the sensitivity and specificity for detecting peaks under different sequencing depths. Next, based on the chromatin accessibility at the single cell level, we developed a peak filtering procedure to further reduce the false positive rate by retaining

only those peaks that were accessible in a significant fraction of the cells compared to background regions. To do so, we first randomly selected 1 million regions from the genome and for each of these regions we calculated the fraction of cells that are accessible. These were used to fit a beta distribution as the null model. We then computed the fraction of accessible cells and its significance level for each candidate peak identified by MACS2. Candidate peaks with FDR < 0.01 were included in the final peak list.

### Generating the union peak set

To compile a union peak set, we combined peaks from all clusters and extended the peak summits by 200 bp on either side. Overlapping peaks were then handled using an iterative removal procedure. First, the most significant peak, i.e., the peak with the smallest p value, was kept and any peak that directly overlapped with it was removed. Then, this process was iterated to the next most significant peak and so on until all peaks were either kept or removed due to direct overlap with a more significant peak.

### Computing relative accessibility scores

We define an accessible locus as the minimal genomic region that can be bound and cut by the Tn5 enzyme. We use  $L \subset N$  to represent the set of all accessible loci. We further define a pseudo-locus as the set of accessible loci that relates to each other in certain meaningful way (for example, nearby loci, loci from different alleles). In this example, pseudo-loci correspond to peaks. We use  $\{d_i | d_i \subset L\}$  to represent the set of all pseudo-loci. Let  $a_i$  be the accessibility of accessible locus  $i$ , where  $i \in L$ . We define the accessibility of pseudo-locus  $d_i$  as  $A_i = \sum_{k \in d_i} a_k$ , i.e., the sum of accessibility of accessible loci associated with  $d_i$ . Let  $C_j$  be the library complexity (the number of distinct molecules in the library) of cell  $j$ . Assuming unbiased PCR amplification, then the probability of being sequenced for any fragment in the library is:  $s_j = 1 - \left(1 - \frac{1}{C_j}\right)^{k_j}$ , where  $k_j$  is the total number of reads for cell  $j$ . If we assume that the probability of a fragment present in the library is proportional to its accessibility and the complexity of the library, then we can deduce that the probability of a given locus  $i$  in cell  $j$  being sequenced is:  $p_{ij} \propto a_i C_j s_j$ . For any pseudo-locus  $d_i$ , the number of reads in  $d_i$  for cell  $j$  follows a Poisson binomial distribution, and its mean is  $m_{ij} = \sum_{k \in d_i} p_{kj} \propto C_j s_j \sum_{k \in d_i} a_k = C_j s_j A_i$ . Given a pseudo-locus (or peak) by cell count matrix  $O$ , we have:  $\sum_j O_{ij} = \sum_j m_{ij}$ . Therefore,  $A_i = Z \frac{\sum_j O_{ij}}{\sum_j C_j s_j}$ , where  $Z$  is a normalization constant. When comparing across different samples the relative accessibility may be desirable as they sum up to a constant, i.e.,  $\sum_i A_i = 1 \times 10^6$ . In this case, we can derive  $A_i = \frac{\sum_j O_{ij}}{\sum_j O_{ij}} * 10^6$ .

### Assigning cell types to cell clusters

To annotate the cell clusters, we first curated a set of marker genes from the PanglaoDB (Franzén et al., 2019) corresponding to expected cell types. We aggregated open chromatin fragments from each cluster and utilized the promoter accessibility, defined as RPM of  $\pm 1$  kb around TSS, as the proxy for gene activity. We then computed the raw cell type enrichment score as the logarithm of the geometric mean of marker genes' activity. The final enrichment scores were obtained by applying two rounds of z-score transformation, first across cell types and then across cell clusters, on raw enrichment scores. For each cluster, we picked the cell type that showed strongest enrichment to make initial assignments. Finally, we manually reviewed these assignments and made adjustments based on focused consideration of marker gene accessibility in conjunction with information about tissue(s) of origin.

### Identification of cell type-restricted peaks

We used a Shannon entropy-based method (Schug et al., 2005) to identify cell type-specific peaks. Given the relative accessibility scores of a peak across clusters, we first converted the scores to probabilities:  $p_i = q_i / \sum_i q_i$ . The entropy was then calculated by:  $H_p = - \sum_t p_t \log_2(p_t)$ . The specificity score is  $Q_{p|t} = H_p - \log_2(p_t)$ . To estimate the statistical significance of specificity scores, we assumed that under the null hypothesis each peak has an average accessibility level across all cell types and that the log base 2 of the cell-type-dependent fold changes from the average level follow a normal distribution with mean equal to zero and standard deviation  $s$ . The value of  $s$  was estimated using the top 50% least variable peaks, and 500,000 samples were then drawn to form the empirical distribution of  $Q_p$  that are used to determine the p values of specificity scores. The cell-type-restricted peaks were then identified using a p value cutoff of 0.025.

### Cell-type enrichment analysis of fine-mapped GTEx eQTLs

The fine-mapped eQTLs (GTEx Analysis V8) in each of the 49 tissues or cell lines were downloaded from the GTEx portal (<http://gtexportal.org/home/index.html>). For each tissue, we first identified the overlapping cCREs with its eQTLs. We then calculated the average of log-transformed accessibility scores of these peaks in each of the 111 cell types. This yielded a tissue by cell-type table containing raw cell-type enrichment scores of eQTLs from each tissue. The raw enrichment scores were then normalized row-wise using z-score transformation. For each tissue, we define the maximum cell-type enrichment as the largest value of z-scores

across 111 cell types. In general, we found that homogeneous tissues tend to have higher maximum cell-type enrichment than tissues that are more heterogeneous.

#### Differential peak analysis

To carry out differential peak analysis between foreground set and background set, we first removed all peaks with fold changes of relative accessibility less than 2. For each peak, we then built a full model and a reduced model.

$$\log \frac{P_{full}}{1 - P_{full}} = \beta_0 + \beta_1 r + \beta_2 c$$

$$\log \frac{P_{reduced}}{1 - P_{reduced}} = \beta_0 + \beta_1 r$$

$P_{reduced}$  and  $P_{full}$  represent the likelihood of the reduced model and full model respectively.  $r$  contains the logarithm of number of fragments.  $c$  is categorical variable indicating if the cell comes from foreground or background. We then used a likelihood ratio test framework to determine whether the full model provided a significantly better fit of the data than the reduced model. We selected the sites using a 5% FDR threshold (Benjamini-Hochberg method).

#### Identification of fibroblast core signature and subtype-specific signatures

We first performed pairwise differential peak analysis for the seven fibroblast subtypes. We then defined fibroblast core signature as peaks that are shared by all subtypes and were not called as differentially accessible in any of the pairwise comparison. Likewise, we defined the specific signature for a subtype as peaks that are differentially more accessible in the given subtype for every pairwise comparison.

#### Measuring the similarity of chromatin accessibility profiles between cell types identified by sci-ATAC-seq and bulk biosamples

We downloaded bulk DNase-seq data from the ENCODE portal. We excluded samples collected at embryonic stage or originated from kidney, bladder or brain tissues, as we did not perform experiments on those tissues. As a result, 638 datasets were kept for downstream analysis. For each of the DNase-seq datasets, we calculated its Pearson correlation coefficient with 111 identified cell types based on RPKM values at identified cCREs. These correlation scores were then scaled using z-score transformation across 111 cell types. We used the maximum of scaled correlation scores to represent each biosample's overall similarity with sci-ATAC-seq cell types.

#### Identification of cCRE modules

A cCRE module is defined as co-accessible regions that share similar accessibility pattern across cell types. To identify cCRE modules, we first performed quantile normalization on the log2 transformed matrix containing accessibilities of 1,154,611 cCREs in 222 fetal and adult cell types. For each cCRE, we then divided its accessibility vector by the L2 norm, which allowed us to better extract the accessibility pattern from the data. Next we applied the k-mean algorithm to this matrix to identify clusters of cCREs. Using the “elbow” method, we determined the number of clusters to be 150.

#### Motif enrichment analysis

We measured the enrichment of 1565 human TF motifs consisting of the JASPAR (2018) core non-redundant vertebrate motifs, the HOCOMOCO v1156 human motif set and the SELEX motifs by Jolma et al.. We computed the enrichments for each of the 1565 motifs relative to a joint cCRE background and filtered the list using FDR cutoff 0.01. For each motif. We reported the motif with the highest enrichment for each of the 286 previously identified motif archetypes ([Vierstra et al., 2020](#)).

#### Identification of candidate driver TFs

We used the Taiji pipeline ([Zhang et al., 2019](#)) to identify candidate driver TFs in each cell cluster. Briefly, for each cell type cluster, we constructed the TF regulatory network by scanning TF motifs at the accessible chromatin regions and linking them to the nearest genes. The network is directed with edges from TFs to target genes. The genes' weights in the network were determined based on the relative accessibility of their promoters. The weights of the edges were calculated by the relative accessibility of the promoters of the source TFs. We then used the personalized PageRank algorithm to rank the TFs in the network.

#### Integration of adult and fetal datasets

To integrate our dataset with the recent cell atlas of fetal chromatin accessibility ([Domcke et al., 2020](#)), we downloaded the fragment files for 63 fetal samples spanning 15 tissues and converted the genomic coordinates from GRC37 (hg19) to GRCh38 using the UCSC liftOver tool. We then performed the quality control, cell filtering and cell clustering using the same pipeline described above and

identified 111 fetal cell types. Next, we combined the QC passed cells from adult and fetal datasets and performed the joint embedding using the SnapATAC algorithm. We considered fetal or adult cells as belonging to different batches, and used a linear model to remove technical batch effects for each dimension in the reduced dimensional space. Using these batch-corrected lower-dimensional representations, we applied the UMAP algorithm to visualize the cells in a 2D space and used the FASTME algorithm (Guindon and Gascuel, 2003) to construct the phylogenetic tree for adult and fetal cell types.

#### Differential peak analysis between fetal and adult cells

To perform differential peak analysis between fetal and adult samples, we modified the likelihood-ratio test framework described above to account for technical batch effects between two datasets. We started with three set of cells. The first two sets of cells corresponded to foreground and background sets that are subject to the differential test. The third set was the auxiliary set corresponding to remaining cells that were not from the first two sets. The auxiliary set served as a proxy to estimate the batch effects. For instance, when performing differential test between two sub-trees of the phylogenetic tree of fetal and adult cell types, for each sub-tree we randomly sampled an equal number of cells for each cell type in the sub-tree. The cells sampled from one branch were considered as foreground and those from the other were considered as background. The remaining cells did not belong to the two sub-trees form the auxiliary set. For each peak, we then built a full model and a reduced model.

$$\log \frac{P_{full}}{1 - P_{full}} = \beta_0 + \beta_1 r + \beta_2 s + \beta_3 t + \beta_4 c$$

$$\log \frac{P_{reduced}}{1 - P_{reduced}} = \beta_0 + \beta_1 r + \beta_2 s + \beta_3 t$$

$P_{reduced}$  and  $P_{full}$  represent the likelihood of the reduced model and full model respectively.  $r$  contains the logarithm of number of fragments.  $s$  is a categorical variable indicating whether the cell comes from the fetal tissue or the adult tissue.  $t$  indicates whether the cell comes from the auxiliary set.  $c$  indicates whether the cell comes from foreground set. We then used a likelihood ratio test framework to determine whether the full model provided a significantly better fit of the data than the reduced model. We selected the sites using a 1% FDR threshold (Benjamini-Hochberg method).

#### Generation of bigwig tracks

Each Tn5-corrected insertion was extended in both directions by 100 bp to form a 200-bp fragment. We then counted the number of fragments overlapping with each base on the genome and generated a bedgraph file. The bedgraph file was converted to bigwig file using the “bedGraphToBigWig” tool.

#### Linking cCREs to target genes

We downloaded the chromosome interactions called from published promoter capture Hi-C data in 14 human tissues (Jung et al., 2019). In each tissue, we first filtered the chromosome interactions using a lenient p value cutoff of 0.1. We then created the chromosome interaction matrix using the normalized interaction frequency. The interaction matrices from 14 tissues were then averaged to get the final interaction matrix. We applied the Activity-by-Contact (ABC) Model (Fulco et al., 2019) to compute the ABC Score for each cCRE-gene pair as the product of Activity (chromatin accessibility) and Contact (interaction frequency), normalized by the product of Activity and Contact for all other cCREs. We retained all distal cCRE-gene connections with an ABC score greater than 0.015.

#### Stratified linkage disequilibrium (LD) score regression

We used LD score regression (Bulik-Sullivan et al., 2015) v1.0.1 to estimate genome-wide GWAS enrichment for disease and non-disease phenotypes within cell type resolved cCREs (peaks called on each cell cluster via MACS2 (Zhang et al., 2008) using the above parameters). We compiled published GWAS summary statistics for complex diseases (Bentham et al., 2015; Bronson et al., 2016; International Multiple Sclerosis Genetics Consortium, 2019; Cordell et al., 2015; Jansen et al., 2019; Ji et al., 2017; Jin et al., 2016; Luo et al., 2017b; Mahajan et al., 2018; Malik et al., 2018; Michailidou et al., 2017; Nielsen et al., 2018; Nikpay et al., 2015; Okada et al., 2014; Paternoster et al., 2015; Pividori et al., 2019; Sakornsakolpat et al., 2019; Schafmayer et al., 2019; Shadrina et al., 2019; Tachmazidou et al., 2019; Tin et al., 2019; Watanabe et al., 2019; Wiberg et al., 2019; Wuttke et al., 2019) and endophenotypes (Astle et al., 2016; Hoffmann et al., 2018; Kemp et al., 2017; Kilpeläinen et al., 2016; Manning et al., 2012; Saxena et al., 2010; Shrine et al., 2019; Strawbridge et al., 2011; Teumer et al., 2018; Warrington et al., 2019) within European populations. Using cell type resolved cCREs as a binary annotation, we created custom partitioned LD score files by following the steps outlined in the LD score estimation tutorial. As background annotations, we included all baseline annotations in the baseline-LD model v1.2 as well as partitioned LD scores created from all merged cCREs. For each trait, we used LD score regression to then estimate coefficient p value for each cell type relative to the background annotations and used the Benjamini-Hochberg procedure to correct for multiple tests.

**GWAS enrichment analysis**

We downloaded the NHGRI-EBI GWAS catalog (Bunielo et al., 2019) (downloaded from <https://www.ebi.ac.uk/gwas/docs/file-downloads> on July 7, 2021) and pruned the catalog using an approach described previously (Boix et al., 2021). Specifically, for each trait and PMID combination, we ranked associations by their significance (P value) and added SNPs iteratively if they were not within 5 kb of previously added SNPs. We then compiled a compendium of 1,123 well-powered GWAS with 10 or more significant SNPs and over 20,000 cases (14% of 8,219 GWAS publications) that capture over 81,057 GWAS loci.

For each cell type and trait combination, we computed the number of intersections between trait associated SNPs and cell-type associated cCREs. We compared this number with the number of intersections between SNPs and the entire set of cCREs from all cell types, using a hypergeometric test to evaluate the statistical significance of enrichments. To estimate the false discovery rate, we generated 1,000 null GWAS with the same lead SNP set size by randomly shuffling the trait associations across GWAS locations. We then computed the null association P values for each permuted GWAS and used the 0.1% top quantiles as the cut-off.

**Fine mapping**

We performed genetic fine mapping for GWAS of diseases and endophenotypes that had sufficient coverage (i.e., were at least imputed into 1000 Genomes). For GWAS with available fine mapping data, we took 99% credible sets directly from the supplemental tables. For GWAS without available fine mapping data, we calculated approximate Bayes factors (Wakefield, 2009) (ABF) for each variant assuming prior variance  $\omega = 0.04$ . For every trait, we obtained index variants for each locus from the supplemental tables of the respective study. We extracted all variants in at least low linkage disequilibrium ( $r^2 > 0.1$  using the European subset of 1000 Genomes Phase 3) (Auton et al., 2015) in a large window ( $\pm 2.5$  Mb) around each index variant. We calculated posterior probabilities of association (PPA) for each variant by dividing its ABF by the cumulative ABF for all variants within the locus. We then defined 99% credible sets for each locus by sorting variants by descending PPA and keeping variants adding up to a cumulative PPA of 0.99.

**Predicting the effects of noncoding variants on TF binding**

To identify SNPs that affect TF binding, we employed deltaSVM models as described previously (Yan et al., 2021). Briefly, 40 bp sequences centered on each SNP were used as input to 94 previously trained and validated TF models. For each SNP, we predicted the binding scores for both alleles by running “gkmpredict.” A SNP was considered to be bound if the binding score passed the pre-defined threshold for either allele. Among those SNPs, deltaSVM scores were calculated using the “deltasvm.pl” script and SNPs with deltaSVM scores passing the threshold for the corresponding model are predicted to affect TF binding.

**External genome browser track data**

Genome browser tracks displaying ChIP-seq and DNase-seq signal from bulk transverse colon datasets and human primary T cell datasets were downloaded from ENCODE with the following identifiers: ENCSR340MRJ, ENCSR557OWY, ENCSR500QVK, ENCSR792VLP, ENCSR627UDJ, ENCSR902BOX, ENCSR218OEZ, ENCSR222QLW.

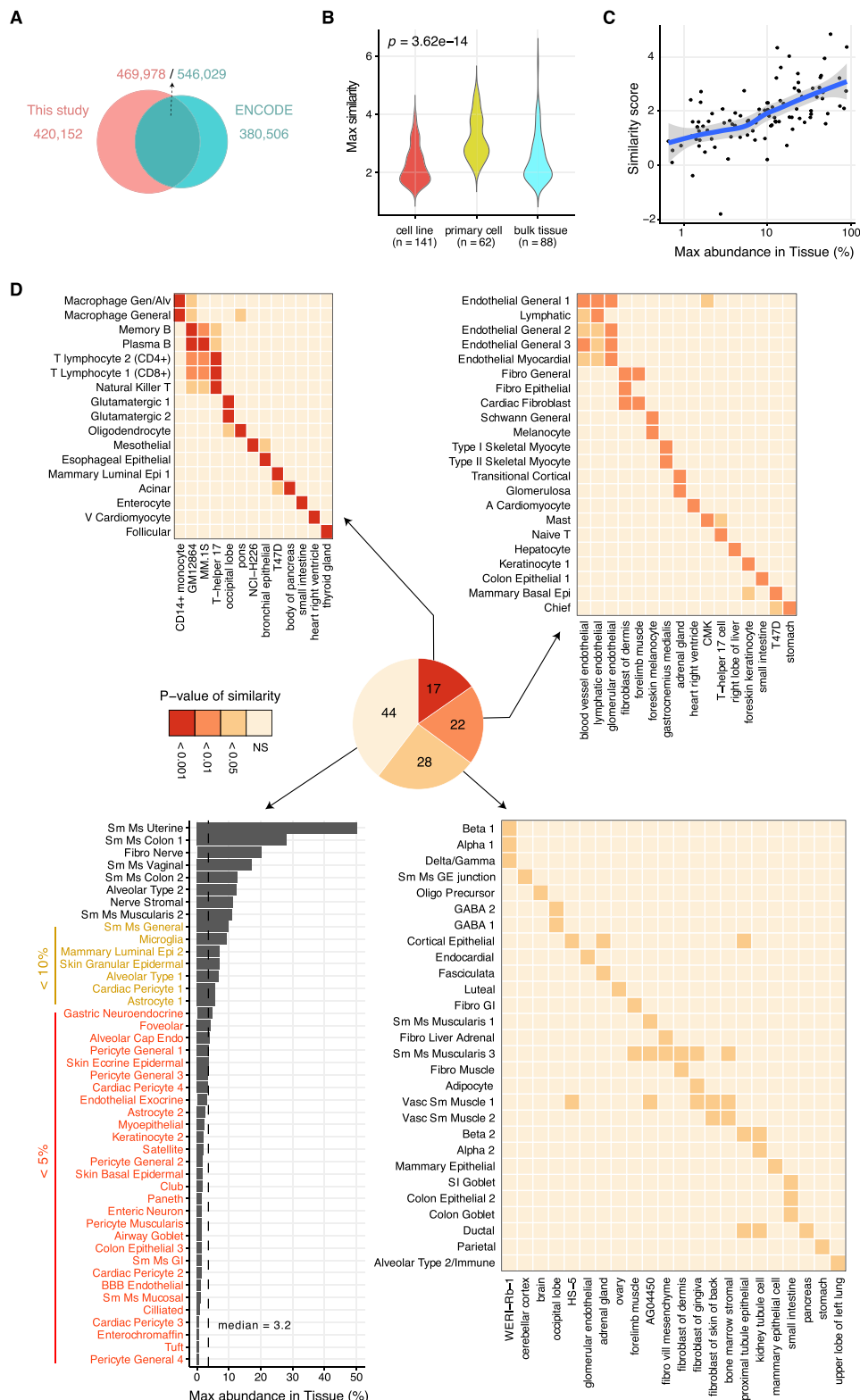
**QUANTIFICATION AND STATISTICAL ANALYSIS**

Statistical parameters were reported either in individual figures or corresponding figure legends. Statistical details of experiments can be found in “[Method details](#).” All statistical analyses were performed in either R or Python.

**ADDITIONAL RESOURCES**

The raw data and analyzed results are available at our interactive web portal: <http://catlas.org/humanenhancer>.

# Supplemental figures

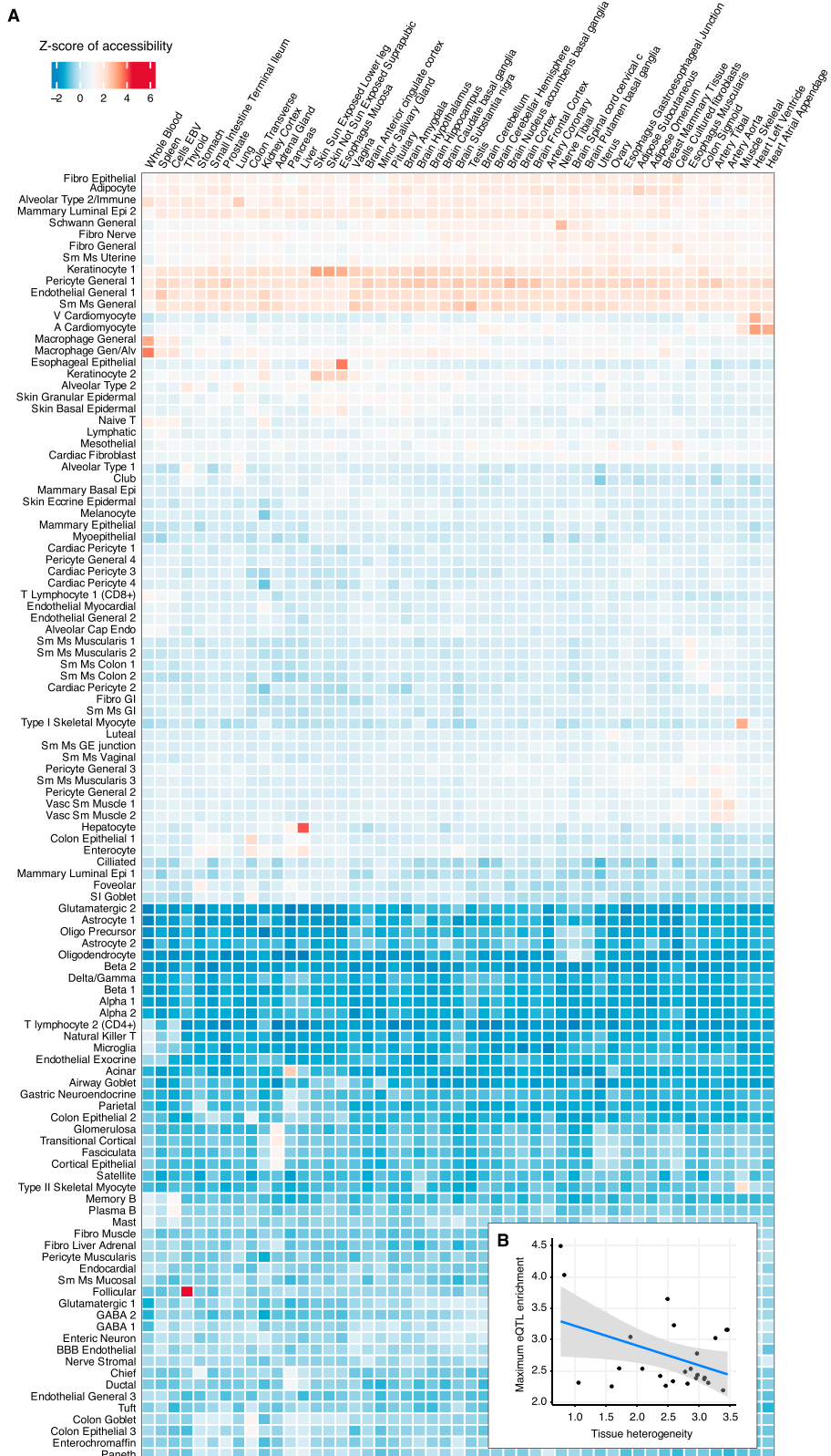


(legend on next page)

---

**Figure S1. Comparison of open chromatin landscapes in adult human cell types from the current study with previous DNase-seq data from bulk biosamples, related to Figure 2**

A) Venn diagram showing the intersection between cCREs identified in the current study with the registry of cCREs created by the ENCODE consortium. B) Distribution of similarity scores for 291 bulk DNase-seq samples stratified by sample classification. Similarity score is defined as the maximum of the standardized correlation scores of a bulk DNase-seq sample with 111 adult human cell types from sci-ATAC-seq. C) Scatterplot showing the similarity score of each cell type as function of its maximal abundance in tissues. Since we did not profile spleen tissue or peripheral blood mononuclear cells, the maximal abundances of immune cell types cannot be accurately estimated and immune cell types were thus excluded from this analysis. D) Pie chart showing similarity between cell types from sci-ATAC-seq and bulk DNase-seq seq samples based on significance level of similarity score. Heatmaps display p values of similarity scores between sci-ATAC-seq cell types and bulk DNase-seq seq samples for each category, bar chart displays maximum abundance across all tissues for each cell type with no significant correlation to a bulk DNase-seq sample. NS = not significant.



*(legend on next page)*

---

**Figure S2. Enrichment of GTEx tissue eQTLs in human cell type cCREs, related to Figure 2**

A) Z-scores for enrichment of GTEx eQTLs from corresponding bulk tissues in cCREs from each sci-ATAC-seq cell type. (B) The chromatin accessibility enrichment of GTEx tissue eQTLs in each tissue was computed as described in STAR Methods, and the maximum value across the 25 matching tissue types was used for the plot.

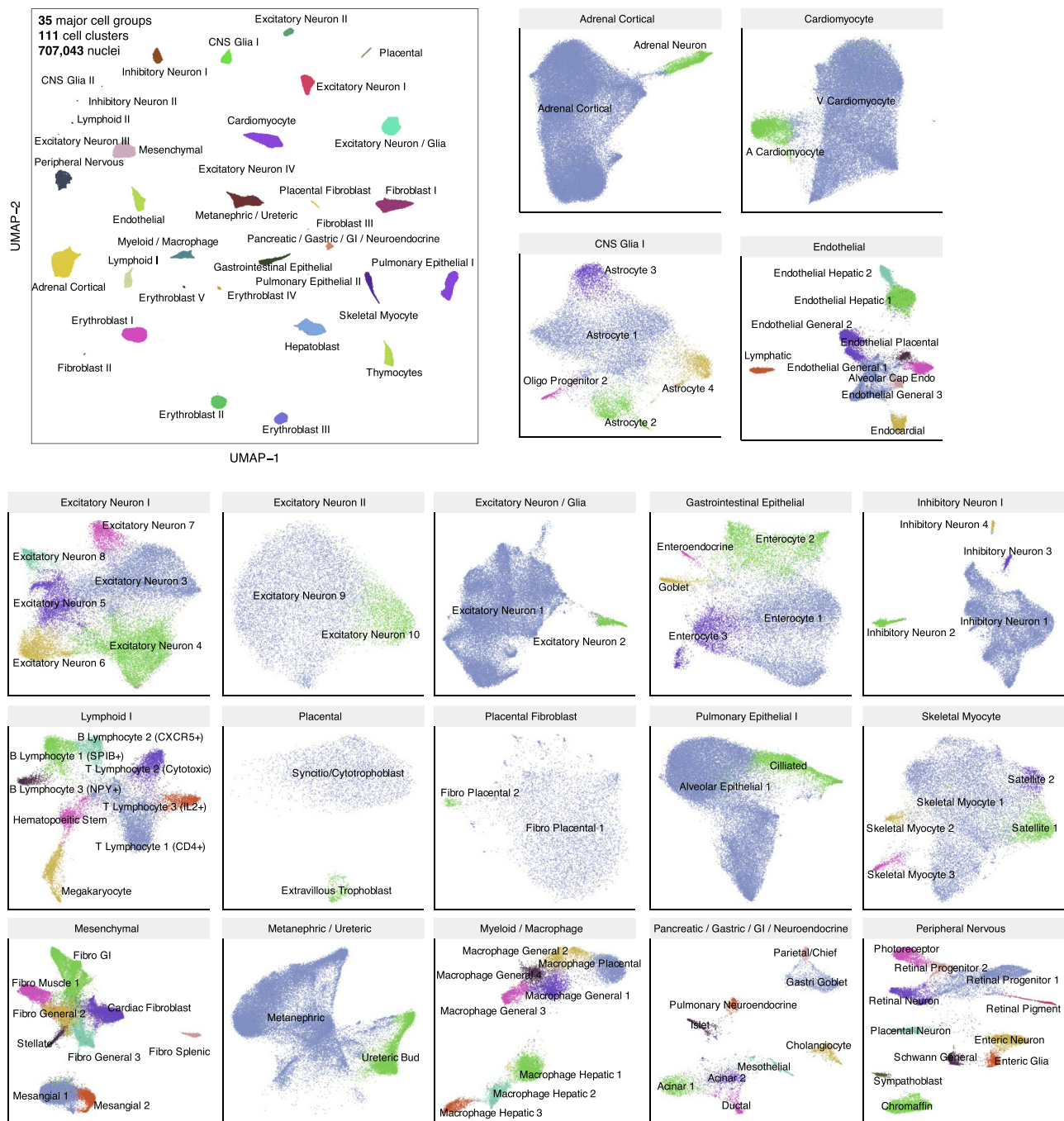
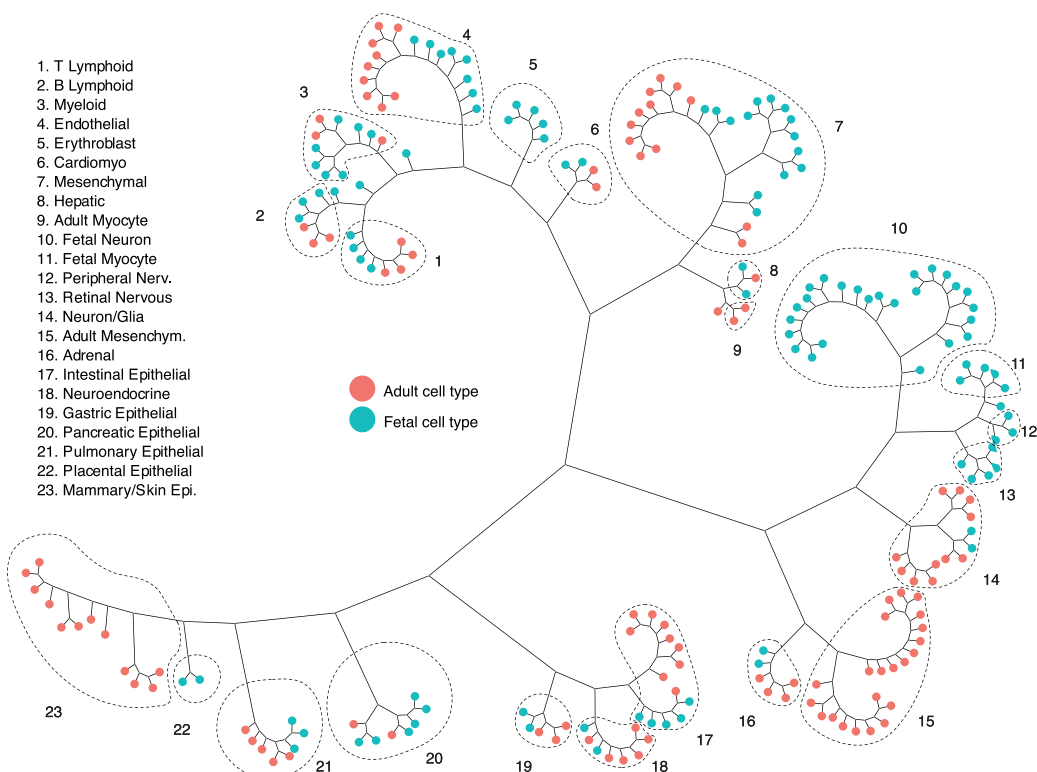


**Figure S3.** Clustering analysis of sci-ATAC-seq data from 15 fetal tissues, related to Figure 3

Each scatterplot shows the UMAP embedding of nuclei from one of 35 major cell groups. Subclusters are indicated by different colors. Subclustering is displayed for 19 out of 35 major cell groups that had more than one subcluster.

**A**

- 1. T Lymphoid
- 2. B Lymphoid
- 3. Myeloid
- 4. Endothelial
- 5. Erythroblast
- 6. Cardiomyo
- 7. Mesenchymal
- 8. Hepatic
- 9. Adult Myocyte
- 10. Fetal Neuron
- 11. Fetal Myocyte
- 12. Peripheral Nerv.
- 13. Retinal Nervous
- 14. Neuron/Glia
- 15. Adult Mesenchym.
- 16. Adrenal
- 17. Intestinal Epithelial
- 18. Neuroendocrine
- 19. Gastric Epithelial
- 20. Pancreatic Epithelial
- 21. Pulmonary Epithelial
- 22. Placental Epithelial
- 23. Mammary/Skin Epi.



**B**

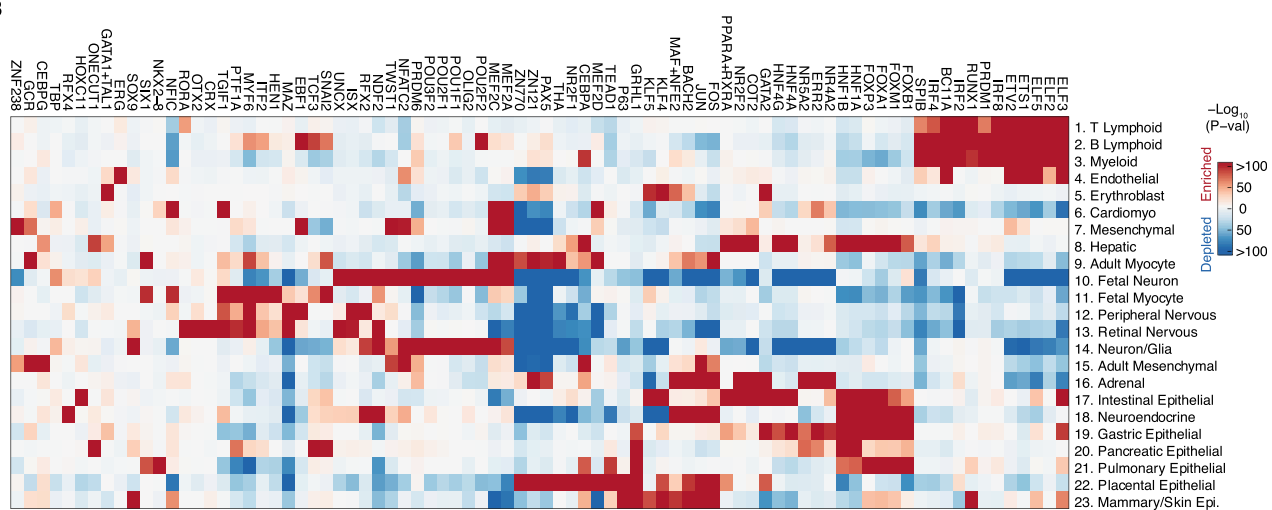


**Figure S4. Phylogenetic analysis of fetal and adult cell types, related to Figure 3**

A) Phylogenetic tree showing relationship between fetal and adult cell types. The tree was constructed using the FASTME algorithm. The distance between two cell types was calculated in the batch-corrected low-dimensional space, and defined as the average Euclidean distance of cell pairs from the two populations. Leaf nodes are colored by life stage. (B) Heatmap showing the TF motif enrichments in cCREs that distinguish clades labeled in Panel (A). Color represents  $-\log_{10}P$ . Only the most enriched TF motif in each of the previously identified motif archetypes (Vierstra et al., 2020) was selected as the representative and the top 5 motifs were selected for each group. Full GO and motif enrichments are available to download on Mendeley Data: 10.17632/yv4fvz6cnm.1.

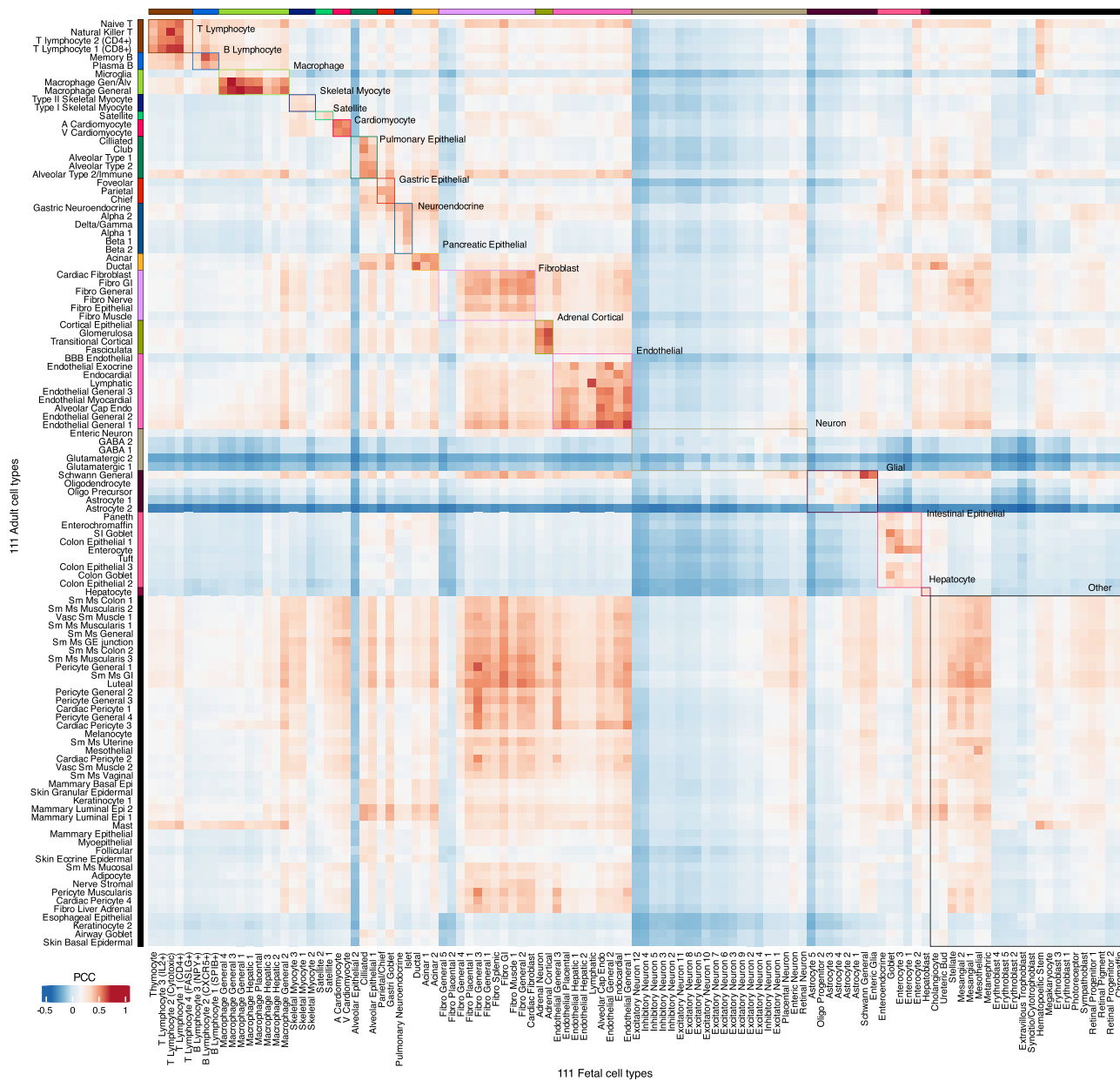


**Figure S5.** Comparison between fetal and adult cell types, related to Figure 3

Heatmap showing Pearson correlation coefficients (PCC) between chromatin accessibility at the 1.2 million cCREs annotated in the current study in 111 adult cell types and 111 fetal cell types. Major cell groups are indicated in boxes.

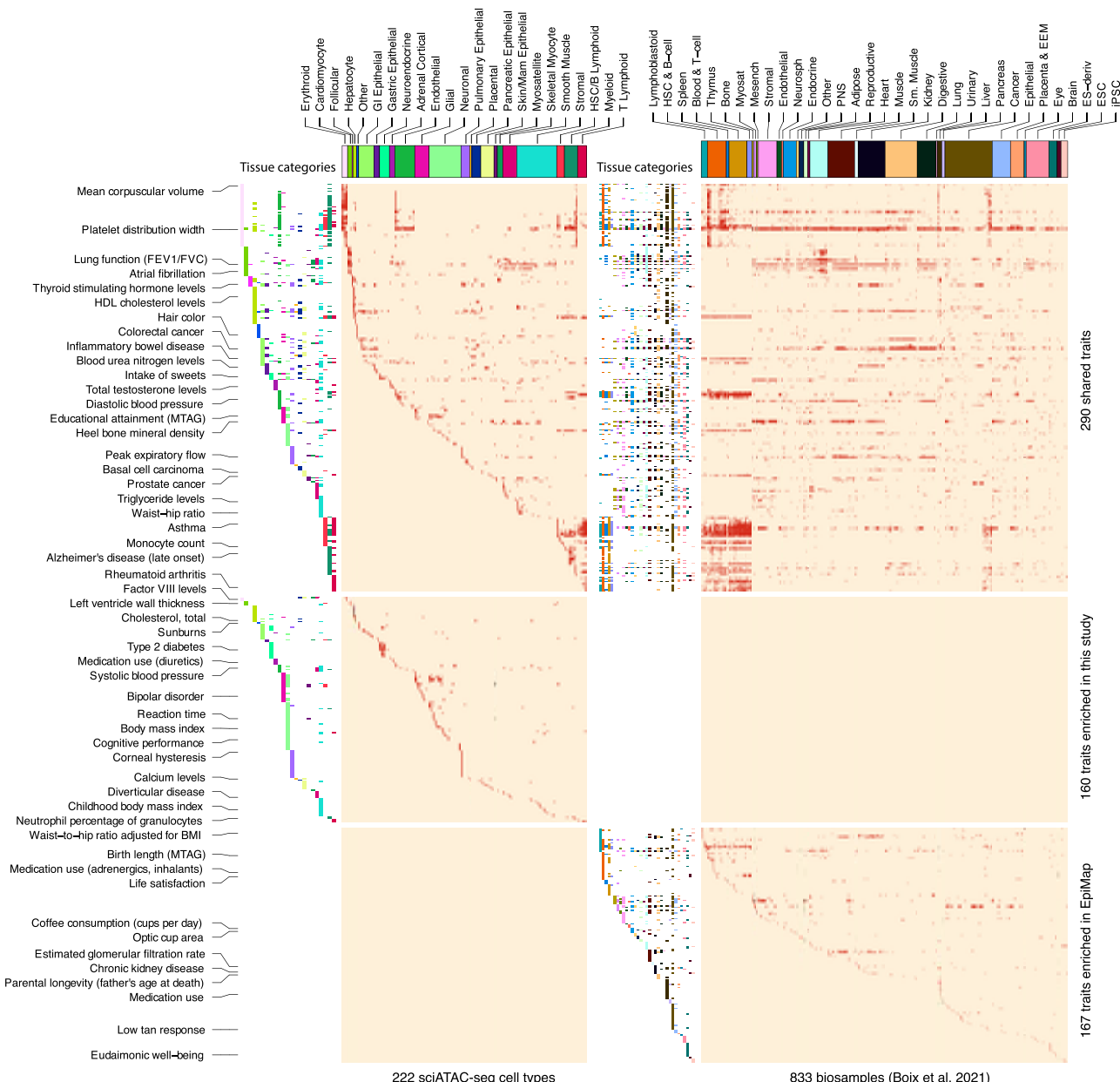
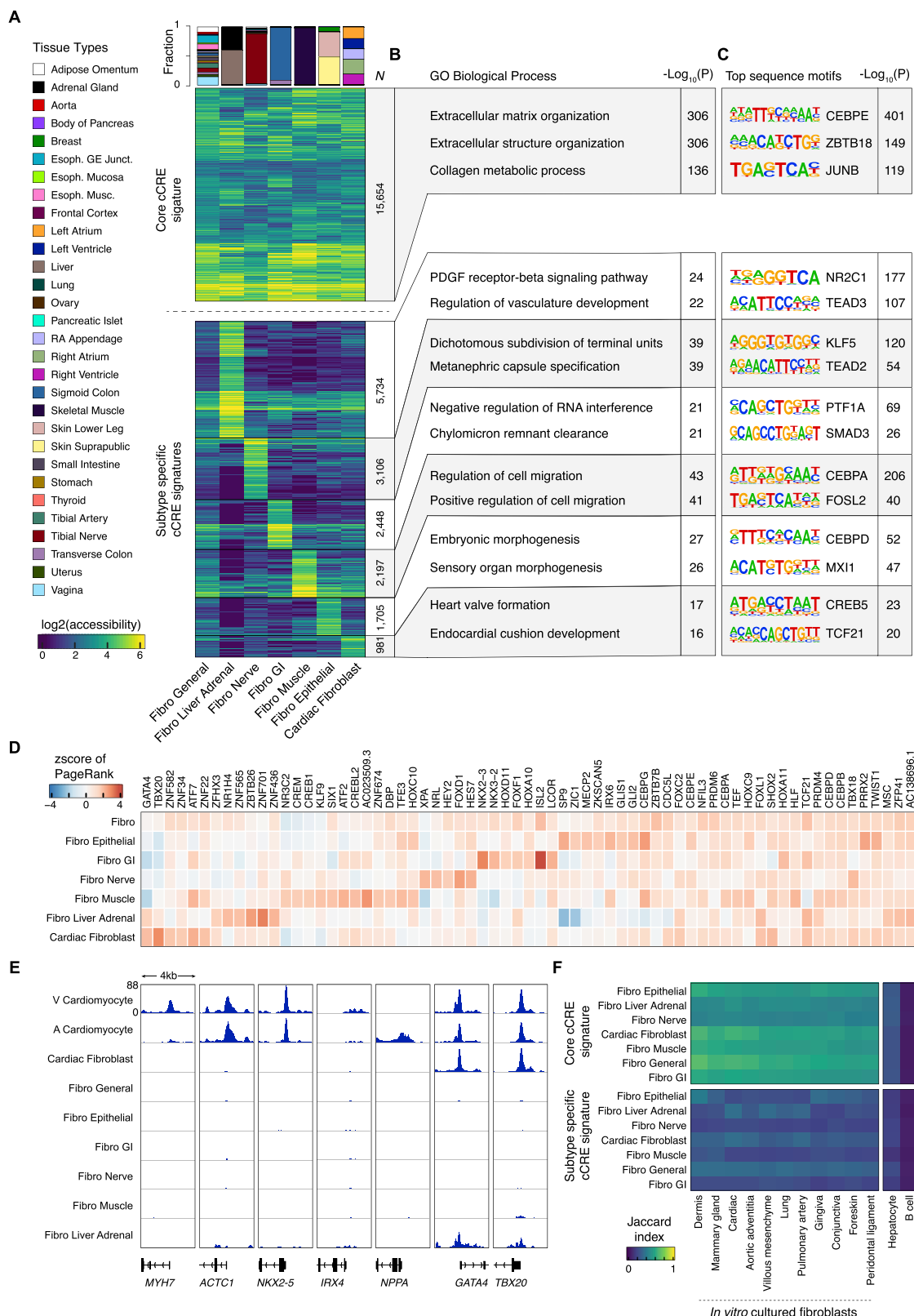


**Figure S6. GWAS variant enrichment analysis with single-cell cCRE atlases and EpiMaps, related to Figure 6**

Heatmap showing significant hypergeometric enrichments (FDR < 0.1%) of index variants from 617 traits downloaded from the NHGRI-EBI catalog (Bunielo et al., 2019) (rows) within cCREs identified from 222 fetal and adult cell types from the current study (left column) and 833 aggregated epigenomic datasets from bulk tissues, cell lines, and primary cells compiled by Boix et al. (2021) (right column). The data underlying the heatmap are available to download on Mendeley Data: 10.17632/yv4fzv6cnm.1.



(legend on next page)

---

**Figure S7. Chromatin features of fibroblasts in different tissue environments, related to Figure 6**

(A) Heatmap representation of core fibroblast cCREs and fibroblast subtype-specific elements. Color represents  $\log_2(\text{accessibility})$ . Bar plot on the top indicates tissues of origin by percentage for each fibroblast subtype. All subtypes showed comparable chromatin accessibility at a set of core fibroblast cCREs, each also showed subtype-specific chromatin accessibility patterns, which were enriched for biological process ontology terms that suggested potential subtype-specific functions. (B) Top GREAT biological process ontology enrichments (McLean et al., 2010) for core fibroblast and fibroblast subtype-specific cCREs. (C) *De novo* sequence motifs and their matched known TF motifs identified by HOMER (Heinz et al., 2010). (D) Heatmap representation showing key TFs (row) in each fibroblast subtype (column) revealed using transcription regulatory network analysis. Color represents standardized PageRank scores. (E) Genome browser tracks for cardiomyocytes and fibroblast subtypes from sci-ATAC-seq at several cardiomyocyte marker genes. Notably, cardiac fibroblasts were accessible at loci encoding cardiac developmental transcription factors GATA4 and TBX20 (Perrino and Rockman, 2006; Shen et al., 2011; Singh et al., 2005), but at other cardiomyocyte marker genes suggesting cardiogenic gene programs in cardiac fibroblasts (Furtado et al., 2014). (F) Similarity indices between (top) core fibroblast cCREs and (bottom) subtype-specific cCREs with *in vitro* cultured fibroblast DNase-seq datasets, and non-fibroblast DNase-seq datasets. All fibroblast subtypes from the current study showed similarity to *in vitro* fibroblasts based on core fibroblast cCRE signatures, but minimal similarity based on subtype-specific fibroblast cCRE signatures suggesting that fibroblast subtype-specific signatures are environment dependent and may be lost during *in vitro* culturing.

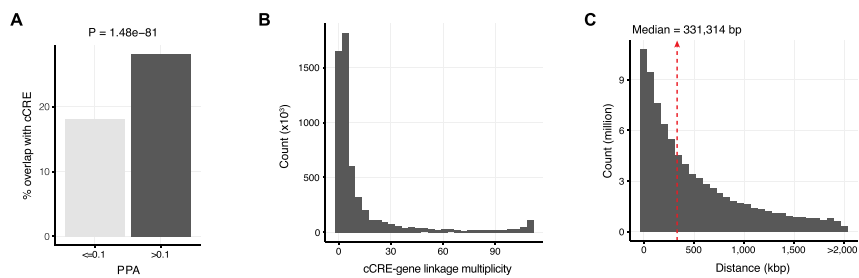


**Figure S8. Characterization of fine mapped risk variants, related to Figure 7**

A) Bar graph showing the percentage of likely causal (Posterior Probability of Association; PPA > 0.1) fine mapped GWAS variants from 48 traits and diseases that overlap the union set of cCREs in adult cell types in the present study. Fisher's exact test was used to compute statistical significance. (B) Histogram showing the multiplicities of cCRE-gene linkage (number of cell types having the linkage). (C) Histogram showing distances in kilobase pairs (kbp) for distal cCRE-to-gene linkages from Activity by Contact (ABC) analysis (Fulco et al., 2019) (ABC score > 0.015).